



NTNU – Trondheim
Norwegian University of
Science and Technology

Unsteady RANS Simulation of Flow around Rectangular Cylinders with different Aspect Ratios at High Reynolds Number

Sindre Misund Dahl

Marine Technology

Submission date: June 2014

Supervisor: Dag Myrhaug, IMT

Co-supervisor: Muk Chen Ong, MARINTEK

Norwegian University of Science and Technology
Department of Marine Technology



MASTER THESIS IN MARINE TECHNOLOGY

SPRING 2014

FOR

STUD. TECHN. SINDRE MISUND DAHL

**UNSTEADY RANS SIMULATION OF FLOW AROUND RECTANGULAR
CYLINDERS WITH DIFFERENT ASPECT RATIOS AT HIGH REYNOLDS
NUMBER**

Rectangular cylinders with large aspect ratios are often found in subsea and offshore structures, e.g., subsea protection structures, subsea drilling templates, and pontoon of semi-submersible platforms. These structural components are often subject to high Reynolds number flows. These high Reynolds number flow conditions are hard and expensive to achieve in an experimental setup, which requires appropriate experimental facilities, incompressible flow, minimizing human and experiment errors during measuring hydrodynamic quantities etc. Therefore an attractive alternative is to use Computational Fluid Dynamics (CFD) to obtain the essential hydrodynamic quantities needed for engineering design.

The student shall:

1. Give a background of CFD and flow around bluff bodies
2. Describe the computational tools
3. Give a background description of turbulence modelling
4. Perform numerical simulation of the flow around rectangular cylinders with different aspect ratios at high Reynolds number
5. Present results and discussion

The work scope may prove to be larger than initially anticipated. Subject to approval from the supervisor, topics may be deleted from the list above or reduced in extent.

In the thesis the candidate shall present his personal contribution to the resolution of problem within the scope of the thesis work.

Theories and conclusions should be based on mathematical derivations and/or logic reasoning identifying the various steps in the deduction.

The candidate should utilize the existing possibilities for obtaining relevant literature.

The thesis should be organized in a rational manner to give a clear exposition of results, assessments, and conclusions. The text should be brief and to the point, with a clear language. Telegraphic language should be avoided.

The thesis shall contain the following elements: A text defining the scope, preface, list of contents, summary, main body of thesis, conclusions with recommendations for further work,

list of symbols and acronyms, reference and (optional) appendices. All figures, tables and equations shall be numerated.

The supervisor may require that the candidate, in an early stage of the work, present a written plan for the completion of the work. The plan should include a budget for the use of computer and laboratory resources that will be charged to the department. Overruns shall be reported to the supervisor.

The original contribution of the candidate and material taken from other sources shall be clearly defined. Work from other sources shall be properly referenced using an acknowledged referencing system.

The thesis shall be submitted:

- Signed by the candidate
- The text defining the scope included
- In bound volume(s)
- Drawings and/or computer prints which cannot be bound should be organized in a separate folder.

Advisors: Dr. Muk Chen Ong, Marintek
Professor Dag Myrhaug

Deadline: 10.06.2014



Dag Myrhaug
Supervisor

The Grid

The grid
A digital frontier

I tried to picture clusters of information
As they moved through the computer
What do they look like?
Ships, motorcycles

Where the circuits like freeways
I kept dreaming of a world
I thought I'd never see

And then, one day
I got in

Homem-Christo et al. (2010)

Preface

This thesis ends my five-year Master of Technology education in Marine Technology at the Norwegian University of Science and Technology (NTNU) in Trondheim.

Several persons have helped me during the thesis work.

I want to thank my advisors Professor Dag Myrhaug at the Department of Marine Technology and Dr. Muk Chen Ong at MARINTEK for their assistance. Especially Dr. Ong has provided great support and interesting conversations.

I would like to thank Håvard Holm for providing me admission to the NTNU supercomputer Vilje. Most of the simulations performed in this project have been run on this computer. I would also like to thank the HPC group at NTNU for keeping the system up and running. The system has been of great importance for my study.

Last, but not least, I would like to thank my family and friends for supporting me through these five years. A special thanks to the guys in the office ÆLITEN.

Trondheim, *June 10, 2014*

A handwritten signature in black ink, reading "Sindre Dahl", written over a horizontal dotted line.

Sindre Misund Dahl

Abstract

Computational Fluid Dynamics (CFD) has been used to evaluate essential hydrodynamic quantities and flow structures around rectangular cylinders with different chord length to depth ratios (aspect ratios) at high Reynolds number. The mean drag coefficient, the root mean square (RMS) value of the lift coefficient, the Strouhal number and flow structures such as vorticity contours, streamlines, pressure distribution and mean streamwise velocity distribution have been predicted.

A two-dimensional Unsteady Reynolds-averaged Navier-Stokes (URANS) model is used together with the standard high Reynolds number $k - \varepsilon$ turbulence model. All simulations have been performed at Reynolds number (based on height) $Re_D = 2 \times 10^5$. The open source CFD code *OpenFOAM* is adopted in the study.

The rectangular cylinder with aspect ratio 5 has been used for the purpose of validating the applicability of the 2D URANS model with the standard high Reynolds number $k - \varepsilon$ turbulence model. Mesh and time step convergence studies have been performed. For the final refinement of the mesh the relative change for $\overline{C_D}$ was less than 0.019%, the relative change for C_{Lrms} was less than 1.30%, while the relative change for the Strouhal number stayed unchanged. For the time step tests the relative change was less than 0.073% for $\overline{C_D}$ and less than 0.80% for C_{Lrms} , while the Strouhal number stayed unchanged. Hence, a case with sufficient numerical accuracy was found. The hydrodynamic quantities were found to be: $\overline{C_D} = 1.1008$, $C_{Lrms} = 0.2760$ and $St = 0.1221$. The results were in good agreement with the published experimental and numerical results. Small deviations were found for the pressure distribution over the cylinder surface. It was concluded that the present numerical model is capable of predicting the flow around the rectangular cylinder with $B/D = 5$ in both quantitative and qualitative manners.

Grid convergence studies and time step tests have been performed for rectangular cylinders of aspect ratio 1, 2, 3, 4 and 5. The present simulations were able to provide satisfactory spatial and time resolutions for all the five aspect ratios at $Re_D = 2 \times 10^5$. The results calculated have reproduced the physics in a reasonable

manner. The drag coefficients were found to be in the range of $1.1 \leq \overline{C_D} \leq 2.1$, the RMS values of the lift coefficients were in the range of $0 \leq C_{Lrms} \leq 1.4$, while the Strouhal numbers alternated between 0.1221 and 0.1373. Reattachment was present for aspect ratio 4 and 5. The mean drag coefficients were found to be in a good agreement with both 2D and 3D numerical simulations, and experiments found at lower Reynolds numbers, while disparities were present for C_{Lrms} and St .

Published work at $Re_D = 2 \times 10^5$ are only found for aspect ratio 5. For the rectangular cylinders with aspect ratio 1, 2, 3 and 4 the lack of published work at the same Reynolds number has made it difficult to perform a detailed validation of the model. More experimental data are required for a further validation study. From the data, it may be concluded that the results from the present study can be useful for engineering design purposes.

Sammendrag

“Computational Fluid Dynamics” (CFD) har blitt brukt til å utrede vesentlige hydrodynamiske størrelser og strømstrukturer rundt rektangulære sylindere med ulike sideforhold (kordelengde/dybde-forhold) ved høyt Reynolds nummer. Den gjennomsnittlige motstandskoeffisienten, den kvadratiske gjennomsnittsverdien av løftkoeffisienten, Strouhalnummeret, og strømstrukturer som virvlingskonturer, strømlinjer, trykkfordeling og gjennomsnittlig horisontal hastighetsfordeling har blitt beregnet.

En todimensjonal “Unsteady Reynolds-averaged Navier-Stokes” (URANS) modell er brukt sammen med den standardiserte høyt-Reynoldsnummer $k-\varepsilon$ modellen. Alle simuleringer har blitt gjennomført med et Reynoldsnummer (definert med dybde) lik $Re_D = 2 \times 10^5$. Den åpne CFD kildekoden *OpenFOAM* er anvendt i studien.

Den rektangulære sylindere med sideforhold lik 5 har blitt brukt med den hensikt å validere anvendelsen til den todimensjonale URANS modellen med standard høyt-Reynoldsnummer $k-\varepsilon$ modellen. Konvergenstudier har blitt gjennomført for rutenett (mesh) og tidssteg. For siste steg i konvergenstudiet av rutenett ble den relative endringen for $\overline{C_D}$ målt til 0.019%, den relative endringen for C_{Lrms} ble målt til 1.30%, mens den relative endringen for Strouhalnummeret forble uendret. For konvergenstudiet av tidssteg ble den relative endringen for $\overline{C_D}$ målt til 0.073%, den relative endringen for C_{Lrms} ble målt til 0.80%, mens den relative endringen for Strouhalnummeret forble uendret. Dette resulterte i et case med tilstrekkelig numerisk nøyaktighet. De hydrodynamiske størrelsene ble funnet å være: $\overline{C_D} = 1.1008$, $C_{Lrms} = 0.2760$ and $St = 0.1221$. Resultatene var i god overensstemmelse med de publiserte eksperimentelle og numeriske resultatene. Små avvik ble funnet i forhold til trykkfordelingen over sylinderoverflaten. Det ble konkludert med at denne numeriske modellen er i stand til å beregne strømning rundt den rektangulære sylindere med sideforhold lik 5.

Konvergenstudier for rutenett og tidssteg har blitt gjennomført for rektangulære

syndere med sideforhold 1, 2, 3, 4 og 5. Tilfeller med tilstrekkelig numerisk nøyaktighet ble funnet for alle fem sideforhold ved $Re_D = 2 \times 10^5$. De kalkulerte resultatene har reprodusert fysikken på en akseptabel måte. Den gjennomsnittlige motstandskoeffisienten var i området $1.1 \leq \overline{C_D} \leq 2.1$, den kvadratiske gjennomsnittsverdien av løftkoeffisienten var i området $0 \leq C_{Lrms} \leq 1.4$, mens Strouhalnummeret vekslet mellom 0.1221 og 0.1373. Fornyet tilkobling mellom separert strøm og sylindere (reattachment) ble observert for rektangulær sylindere med sideforhold lik 4 og 5. De gjennomsnittlige motstandskoeffisientene ble funnet å være i god overenstemmelse med både 2D og 3D numeriske simuleringer, og eksperiment funnet ved lavere Reynoldsnummer, mens uligheter var tilstede i forhold til C_{Lrms} og St .

Publiserte data ved $Re_D = 2 \times 10^5$ er bare funnet for rektangulære sylindere med sideforhold lik 5. For de rektangulære sylindere med sideforhold lik 1, 2, 3 og 4 har mangelen på publiserte data ved likt Reynoldsnummer gjort det vanskelig å gjennomføre en detaljert validering av modellen. Den gjennomsnittlige motstandskoeffisienten var i god enighet med publiserte eksperimentelle og numeriske data funnet ved lavere Reynoldsnummer, mens avvik ble funnet for den kvadratiske gjennomsnittsverdien av løftkoeffisienten og Strouhalnummeret.

Publiserte data for Reynoldsnummer (definert med sylindere høyde) lik $Re_D = 2 \times 10^5$ er bare funnet for rektangulære sylindere med sideforhold lik 5. Det er mangel på publiserte data med likt Reynoldsnummer for rektangulære sylindere med "aspect ratio" lik 1, 2, 3 og 4, og dette har gjort det vanskelig å utføre en detaljert validering av modellen. Fler eksperimentelle data er nødvendig for en videre valideringsstudie. På denne bakgrunn kan det konkluderes med at resultatene fra denne studien skulle være formålstjenelig for prosjekteringsformål.

Contents

1	Introduction	1
1.1	Background	1
1.2	Definition of terms	2
1.3	Published work	2
1.4	Outline of the thesis	5
2	Theory	7
2.1	Vortex shedding	7
2.1.1	Flow regime	7
2.1.2	Vortex shedding	9
2.1.3	Vortex shedding frequency	10
2.2	Forces	11
2.2.1	Forces acting on a cylinder	11
2.2.2	Force coefficients	12
2.2.3	Pressure distribution	12
2.2.4	Effect of cross-sectional shape on force coefficients	13
3	CFD	15
3.1	Introduction	15
3.2	OpenFOAM	16
3.3	Meshing	17
3.3.1	Courant number	17
3.4	Mathematical Description	18
3.4.1	Conservation of mass	18
3.4.2	Conservation of momentum	19
3.5	Turbulence	19
3.5.1	DNS	20
3.5.2	LES	20
3.5.3	RANS	20
3.5.4	DES	22

3.5.5	Law of the wall	22
4	Numerical set-up	25
4.1	Domain	25
4.2	Boundary Conditions	26
4.3	Mesh	28
4.4	OpenFOAM	31
4.5	High Performance Computing - Vilje	31
5	Results and discussion	33
5.1	Validation of the numerical model	33
5.1.1	Results	33
5.1.2	Pressure	36
5.1.3	Velocity distribution	38
5.1.4	Vorticity contours	38
5.1.5	Conclusion	40
5.2	Results	41
5.3	Effect of aspect ratio	42
5.3.1	Forces and Strouhal number	42
5.3.2	Vorticity contours	47
5.3.3	Streamlines	49
5.3.4	Pressure	51
5.3.5	Velocity distribution	55
6	Conclusion	57
7	Recommendations for Further Work	59
	Bibliography	61
	Appendices	I
	Appendix A Simulation Control Files	III
A.1	controlDict	III
A.2	fvSchemes	V
A.3	fvSolution	VI
	Appendix B Pressure distribution	IX
	Appendix C Velocity contours	XI

List of Tables

4.1	Boundary conditions for k , ε and ν_t	28
5.1	Mesh and time convergence study of hydrodynamic quantities for rectangular cylinder with aspect ratio 5	35
5.2	Hydrodynamic quantities for rectangular cylinder with aspect ratio 5	36
5.3	Results from grid convergence study and time step test for rectangular cylinders with aspect ratio 1, 2, 3, 4 and 5	43

List of Figures

1.1	Subsea protection covers and rectangular submerged floating tunnel	1
1.2	Definition of B, D, S and location of base point (bp)	2
2.1	Regimes of flow around a smooth, circular cylinder in steady current	8
2.2	The shear layer	9
2.3	The alternative manner of the vortex shedding	10
2.4	Strouhal number for a smooth circular cylinder	11
2.5	Drag and lift traces obtained from the measured pressure distributions	12
2.6	Pressure distribution at different Re numbers for a smooth cylinder	13
3.1	Structure of OpenFOAM	16
3.2	Mesh classes	18
3.3	Large and small scale motions of turbulent flow and the time dependence of u at a point	20
3.4	Velocity distribution near a solid wall	23
4.1	Computational domain	26
4.2	The block-topology used for building the mesh around a square cylinder	29
4.3	The mesh around a square cylinder	30
5.1	Time history of force coefficients from case A5M1	34
5.2	Mesh convergence of drag and lift coefficient.	35
5.3	Time-averaged pressure distributions on the surfaces of the 5:1 rectangular cylinder	37
5.4	Mean streamwise velocity distribution along the centreline of the 5:1 rectangular cylinder	38
5.5	Vorticity contours from a near to full vortex shedding period of the 5:1 rectangular cylinder	40
5.6	Variation of the mean drag coefficient according to aspect ratio	44

5.7	Variation of the RMS value of the lift coefficient according to aspect ratio	45
5.8	Variation of the Strouhal number according to aspect ratio	45
5.9	Instantaneous vorticity contours at $tU_\infty/D = 300$ for rectangular cylinders with aspect ratio 1, 2, 3, 4 and 5	49
5.10	Schematic overview of mean flow structure	49
5.11	Symmetry in vortices around rectangular cylinder with aspect ratio 3	50
5.12	Asymmetry in vortices around rectangular cylinder with aspect ratio 4	51
5.13	Instantaneous streamlines at $tU_\infty/D = 300$ for rectangular cylinders with aspect ratio 1, 2, 3, 4 and 5	52
5.14	Variation of mean base pressure coefficients according to aspect ratio	53
5.15	Time-averaged pressure distributions on the surfaces of rectangular cylinders with aspect ratio 1, 2, 3, 4 and 5	54
5.16	Variation of length of the mean recirculation region according to aspect ratio	55
5.17	Mean streamwise velocity distribution along the centreline of rectangular cylinders with aspect ratio 1, 2, 3, 4 and 5	56
B.1	Instantaneous pressure contours at $tU_\infty/D = 300$ for the rectangular cylinders with aspect ratio 1, 2, 3, 4 and 5	IX
B.2	Averaged pressure contours for the rectangular cylinders with aspect ratio 1, 2, 3, 4 and 5	X
C.1	Instantaneous velocity contours at $tU_\infty/D = 300$ for rectangular cylinders with aspect ratio 1, 2, 3, 4 and 5.	XI
C.2	Mean velocity contours for rectangular cylinders with aspect ratio 1, 2, 3, 4 and 5.	XII

List of Abbreviations

2D:	Two-Dimensional
3D:	Three-Dimensional
BARC:	Benchmark on the Aerodynamics of a Rectangular 5:1 Cylinder
CFD:	Computational Fluid Dynamics
DES:	Detached Eddy Simulation
DNS:	Direct Numerical Simulation
LES:	Large Eddy Simulation
PISO:	Pressure Implicit with Splitting of Operators
RANS:	Reynolds-averaged Navier-Stokes
RAS:	Reynolds-Averaged Simulation
RMS:	Root mean square
URANS:	Unsteady Reynolds-averaged Navier-Stokes

List of Symbols

δ_{ij} :	Kronecker delta
ε :	Rate of dissipation of turbulent kinetic energy
κ :	von Karmans constant
μ :	Dynamic viscosity of fluid
ν :	Kinematic viscosity of fluid
ν_t :	Turbulent viscosity of fluid
ω :	Instantaneous vorticity
ϕ :	Angular coordinate
ρ :	Density of fluid
σ_k :	Turbulent Prandtl number for kinetic energy
σ_ε :	Turbulent Prandtl number for dissipation
τ_{ij} :	Stress tensor
τ_w :	Wall shear stress
B :	Cylinder chord length
B/D :	Aspect ratio
bp :	Base point
C_D :	Instantaneous drag coefficient
$\overline{C_D}$:	Mean drag coefficient
C_{ε_1} :	Constant in the model equation for ε

C_{ε_2} :	Constant in the model equation for ε
C_L :	Instantaneous lift coefficient
C_{Lrms} :	Root mean square value of the lift coefficient
C_{max} :	Maximum Courant number
C_μ :	Turbulent-viscosity constant in the k- ε model
$\overline{C_p}$:	Average pressure coefficient over cylinder surface
C_{pb} :	Mean base pressure coefficient
D :	Cylinder diameter
D :	Cylinder depth
E :	Log law constant
(L/D) :	Turbulence length scale
F_D :	Instantaneous drag force
$\overline{F_D}$:	Mean drag force
$\overline{F_f}$:	Mean component of the in-line friction force
F_L :	Instantaneous lift force
$\overline{F_p}$:	Mean component of the in-line pressure force
f_ν :	Vortex shedding frequency
g :	Gravitational acceleration
h_p :	Normal distance between first node and the wall
I_u :	Turbulence intensity
k :	Turbulent kinetic energy
p :	Static pressure
p_0 :	Hydrostatic pressure
p_0 :	Inlet pressure

\bar{p} :	Mean pressure
Re :	Reynolds number
Re_B :	Reynolds number based on breadth
Re_D :	Reynolds number based on depth
S :	Coordinate along cylinder surface
St :	Strouhal number
t :	Time
Δt :	Time step
T_v :	Vortex shedding period
U :	Fluid velocity
U_i :	Cartesian component of the velocity vector
\bar{U} :	Mean velocity
U_∞ :	Incident velocity
u^+ :	Dimensionless velocity
$\overline{u'_i u'_j}$:	Reynolds stress component
u_τ :	Friction velocity
Δx :	Element length
X_1 :	Horizontal axis in coordinate system
X_2 :	Vertical axis in coordinate system
x_i :	Cartesian coordinates
y :	Distance from the wall
y^+ :	Dimensionless distance from the wall

1 Introduction

1.1 Background

The developments of the offshore industry have increased the importance of flow-structure interactions around marine structures. Flows around sharp-edged square and rectangular structures are often seen in offshore and subsea engineering. The pontoons of a semi-submersible, the columns of a tension-leg platform and subsea protection structures (see Figure 1.1) are among many exposed sharp-edged structures often subject to high Reynolds number flows.

The submerged floating tunnels are increasingly recognised as a competitor to bridges. The Norwegian Public Roads Administration has been commissioned to investigate the potential of eliminating all ferries along the western corridor (E39) between Kristiansand and Trondheim (Norwegian Public Roads Administration 2012). A big challenge is the fjord crossings, where strong currents are present. One of the main alternatives the team is looking into is the submerged floating tunnel. A suggestion for a rectangular tunnel is shown in Figure 1.1.

It is hard and expensive to achieve these high Reynolds number flow conditions in laboratory testing. Computational Fluid Dynamics (CFD) is therefore an attractive alternative for engineering design.

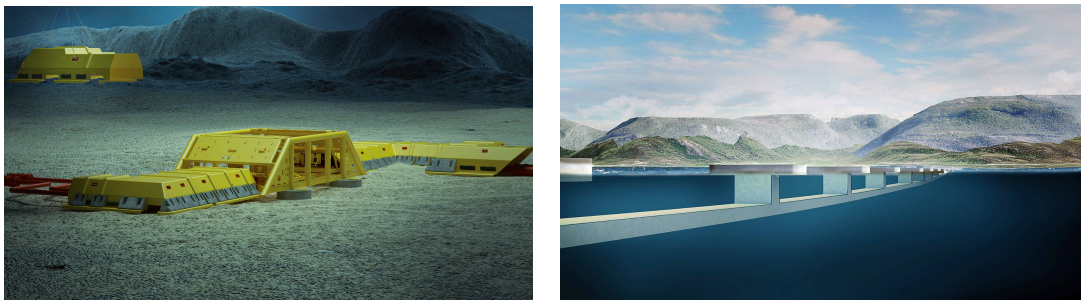


Figure 1.1: Subsea protection covers (left, from (HighComp 2014)) and rectangular submerged floating tunnel (right, from (Teknisk Ukeblad 2012))

1.2 Definition of terms

The dimensions of the rectangular cylinders are B , the chord length along the direction of the flow and D , the depth of the section, as shown in figure 1.2. The cylinder aspect ratio (B/D) is the chord length to depth ratio. The length S is following the cylinder surface from the stagnation point to the cylinder base point, bp . The cylinder is drawn in the X_1X_2 plane.

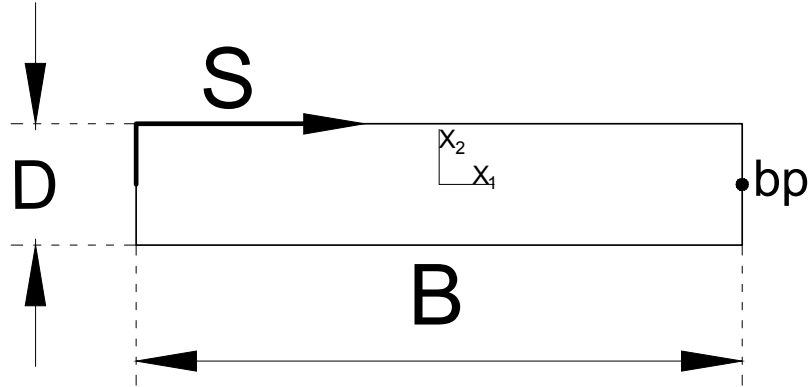


Figure 1.2: Definition of B , D , S and location of base point (bp)

1.3 Published work

There have been high interests in flows around rectangular cylinders with various aspect ratios in both the scientific and engineering communities. The topic is highly relevant for fluid engineering, including both aerodynamics and hydrodynamics. Yet, not many numerical studies have been performed at high Reynolds number, e.g. $Re_D = 2 \times 10^5$.

Lee (1974) measured mean and fluctuating pressure fields acting on a two-dimensional square cylinder in uniform and turbulent flows. The experiments were done in a wind tunnel with Reynolds number 1.76×10^5 . The experiments showed that increasing the turbulence intensity raises the base pressure and therefore also reduces the drag force.

Okajima (1982) investigated the Strouhal number on rectangular cylinders with aspect ratios from 1 to 4. The experiments were in wind and water tunnels with Reynolds number in a range of 70 and 2×10^4 . He found an abrupt change of flow pattern with a sudden discontinuity in the Strouhal-number curves for cylinders

with $B/D = 2$ and 3.

Nakamura & Yoshimura (1982) investigated the Strouhal number on rectangular cylinders with aspect ratio 0.2 to 5 in smooth and turbulent flows. The range of Reynolds numbers based on height were 5.5×10^3 to 1.4×10^5 . They observed that turbulence weakens the torsional vibrations of the cylinders, and eventually suppresses them.

Yu & Kareem (1998) used 2D (two-dimensional) and 3D (three-dimensional) LES to investigate the influence of the aspect ratio on the velocity field around prisms. They found the results to be in good agreement with experimental data found by Sakamoto et al. (1989), performed to inspect the fluctuating forces acting on rectangular cylinders of various aspect ratio, with Reynolds number 5.5×10^4 .

Shimada & Ishihara (2002) used a modified $k-\varepsilon$ turbulence model to investigate the aerodynamic characteristics of rectangular cylinders of infinite length and various breadth-to-depth ratios ranging from $B/D = 0.6$ to 8. They succeeded in reproducing the vortex shedding of flow at $Re_D = 2.2 \times 10^4$, including discontinuity in the Strouhal number at $B/D = 2.2, 2.5, 2.7$ and 6. However, the pressure and force fluctuations were underestimated. The reported results were in good agreement with wind tunnel experiments by Otsuki et al. (1978), performed to investigate uniform flows around rectangular cylinders of aspect ratio 1 to 4 with Reynolds number in the range of 6.5×10^4 to 7.6×10^4 .

A high Reynolds number, external, unsteady flow around a stationary, sharp-edged cylinder with aspect ratio 5 was chosen as a benchmark case for the Benchmark on the Aerodynamics of a Rectangular 5:1 Cylinder (BARC, Bartoli et al. (2008)). The BARC was aimed to deeply investigate one specific external flow problem, to access the consistency of experimental and computational results and to compare the results from different methods.

Schewe (2006, 2009) examined the flow over a broad range of Reynolds numbers ($2 \times 10^4 < Re_B < 2 \times 10^6$) in a high pressure wind-tunnel. The results reported were in good agreement with wind-tunnel experiments performed by Matsumoto (2005) at $Re_D = 4 \times 10^4$.

Bruno et al. (2010) used 3D LES to investigate the flow around a rectangular cylinder of aspect ratio $B/D = 5$ at $Re_D = 4 \times 10^4$. They reported that although the 3D flow features are not negligible, the driving forces on the rectangular cylinder remain 2D.

Mannini et al. (2010) studied the flow around a 5:1 rectangular cylinder with Reynolds numbers 2×10^4 by performing URANS simulations. They found that the unsteady behaviour of the computed flow at low Reynolds number is more complex and less regular than at high Reynolds number.

Ong (2012) applied 2D URANS equations with high Reynolds number $k-\varepsilon$ turbulence model for flows over a wide range of Reynolds number ($Re_B = 5 \times 10^5, 1 \times 10^6, 1.5 \times 10^6$ and 2×10^6). The study concluded that the high Reynolds number $k-\varepsilon$ turbulence model should be reliable and useful as an engineering assessment tool for design work.

Bartoli et al. (2011) highlighted the strong sensitivity of the flow at Reynolds number $Re_D = 4 \times 10^4$ by the use of wind tunnel experiments. They observed a variation of the location of reattachment due to small flow angles.

Mannini et al. (2011) carried out a 3D Detached Eddy Simulation (DES) to investigate the rectangular cylinder at $Re_D = 2.64 \times 10^4$. They commented that the quality of the simulations was improved with respect to 2D and 3D URANS methods, but the requirements lead to a high computational cost. The results reported were in good agreement with wind-tunnel experiments at Reynolds number $Re_D = 4.2 \times 10^4$ performed by Galli (2005).

About 70 realizations of the BARC flow configurations were obtained. Bruno et al. (2014) provided an overview after the first four years of activity of the BARC study. The experimental and numerical realizations were in good agreement in terms of the base pressure, the drag force and the Strouhal number. However, the results had a significant dispersion concerning the standard deviation of the lift coefficient, the distribution of mean pressure and fluctuating pressure and the mean flow features on the cylinder. The authors commented that they were hoping to see the number of flow realizations in the ensemble increased.

The aforementioned summary of the published research work will be served as a literature review for the research work presented in chapter 5.

1.4 Outline of the thesis

Chapter 2 gives a brief review of flow around bluff bodies, the development of vortex shedding and the hydrodynamical forces acting on the bodies.

Chapter 3 describes the basics of CFD, the CFD software used in this thesis, the governing equations and turbulence - including numerical methods for modelling turbulence.

Chapter 4 presents the numerical set-up used in the study - the domain, the boundary conditions, the mesh and the numerical schemes used.

Chapter 5 gives a validation of the numerical model and presents and discusses the results from the study.

Chapter 6 gives a final conclusion of the work carried out in the thesis.

Chapter 7 gives recommendations for further work.

2 Theory

The purpose of the present chapter is to give a brief description of the mechanism of vortex shedding and the computation of hydrodynamical forces. Flows around circular cylinders are the most well documented phenomena in the literature. However, the flow structures around rectangular cylinders are not documented in details. The formation of the vortex shedding mechanism and the force calculation procedure are the general knowledge for flow around bluff bodies. Thus the flow around circular cylinders is elaborated in this section and the differences between circular and rectangular cylinders are pointed out. For a more thorough review of flows around circular cylinders the reader is referred to Sumer & Fredsoe (2006).

2.1 Vortex shedding

2.1.1 Flow regime

A dimensionless quantity used to describe the flow around a smooth circular cylinder is the Reynolds number

$$Re = \frac{U_\infty D}{\nu} \quad (2.1)$$

where U_∞ is the incident velocity, D is the diameter of the cylinder, and ν is the kinematic viscosity of the fluid.

Figure 2.1 illustrates the regimes of flow around a smooth, circular cylinder in steady current. As seen from the figure, the fluid stream separates itself from the surface of the body at sufficiently high Reynolds numbers. No separation occurs for $Re < 5$, while for $Re > 40$ a vortex street downstream of the cylinder is present. For $200 < Re < 300$ a transition to a turbulent wake occurs. For $Re > 300$, the wake is completely turbulent, while as the Reynolds gets increased from $Re = 3.5 \times 10^5$ the boundary layer itself gradually becomes turbulent.






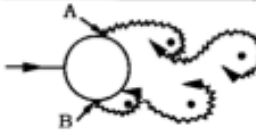
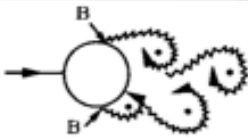
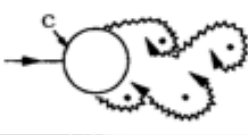

a)		No separation. Creeping flow	$Re < 5$
b)		A fixed pair of symmetric vortices	$5 < Re < 40$
c)		Laminar vortex street	$40 < Re < 200$
d)		Transition to turbulence in the wake	$200 < Re < 300$
e)		Wake completely turbulent. A: Laminar boundary layer separation	$300 < Re < 3 \times 10^5$ Subcritical
f)		A: Laminar boundary layer separation B: Turbulent boundary layer separation; but boundary layer laminar	$3 \times 10^5 < Re < 3.5 \times 10^5$ Critical (Lower transition)
g)		B: Turbulent boundary layer separation; the boundary layer partly laminar partly turbulent	$3.5 \times 10^5 < Re < 1.5 \times 10^6$ Supercritical
h)		C: Boundary layer comple- tely turbulent at one side	$1.5 \times 10^6 < Re < 4 \times 10^6$ Upper transition
i)		C: Boundary layer comple- tely turbulent at two sides	$4 \times 10^6 < Re$ Transcritical

Figure 2.1: Regimes of flow around a smooth, circular cylinder in steady current (from Sumer & Fredsoe (2006))

2.1.2 Vortex shedding

The separation occurring around the cylinder is due to a pressure gradient imposed by the geometry. As a result of the no-slip condition, vorticity is created along the cylinder boundary layer. The layer separates from the cylinder surface to form a free shear layer in the wake, containing the vorticity (see Figure 2.2). The vorticity causes the shear layer to roll up into a vortex. This vortex formation happens on both sides of the cylinder simultaneously. The pair of vortices is unstable, causing one of the vortices to be pulled across the wake, cutting off the other. For the next shedding cycle a vortex is cut off at the other side of the cylinder, rotating in the opposite direction. This alternative manner continues throughout the vortex shedding process, as illustrated in Figure 2.3.

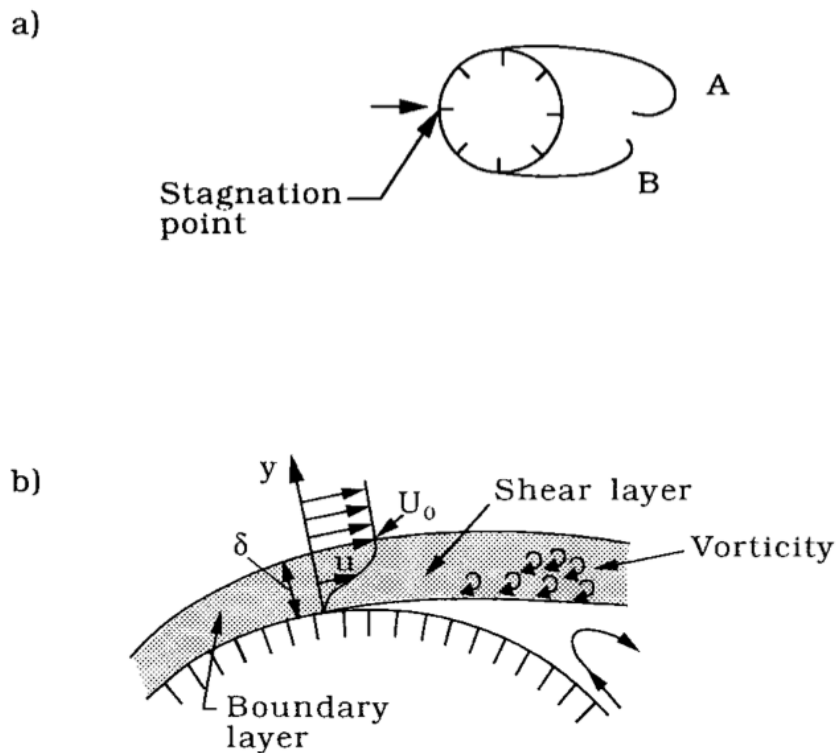


Figure 2.2: The shear layers on both sides roll up to form the lee-wake vortices, vortices A and B (from Sumer & Fredsoe (2006))

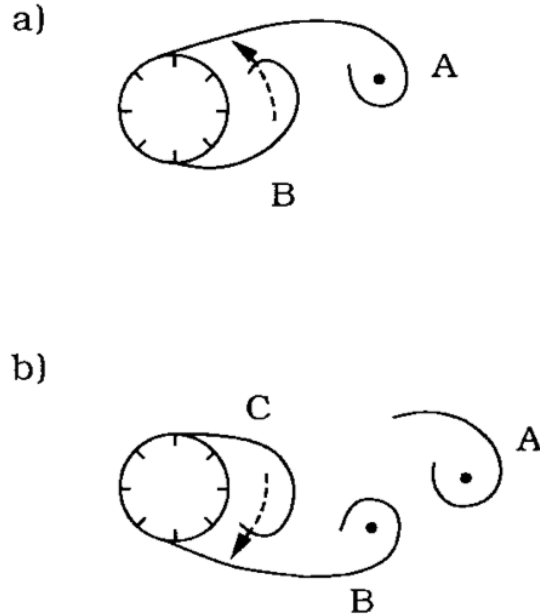


Figure 2.3: The alternative manner of the vortex shedding (from Sumer & Fredsoe (2006))

2.1.3 Vortex shedding frequency

The vortex shedding frequency is often measured through the dimensionless coefficient named Strouhal number. The Strouhal number is defined as

$$St = \frac{f_v D}{U_\infty} \quad (2.2)$$

where $f_v = \frac{1}{T_v}$ is the vortex shedding frequency and T_v the vortex shedding period.

On dimensional grounds the Strouhal number can be seen to be a function of the Reynolds number. For a laminar vortex street the Strouhal number is increasing towards a value of 0.2. It stays near-to constant in the Subcritical domain, but increases rapidly in the critical regime as one of the separation points starts to become turbulent. The decrease in the Supercritical regime is a result of the change of position for the separation points. A drop occurs when it reaches the Upper transition (as the boundary layer is completely turbulent at one side). Figure 2.4 illustrates how the Strouhal number varies with Re.

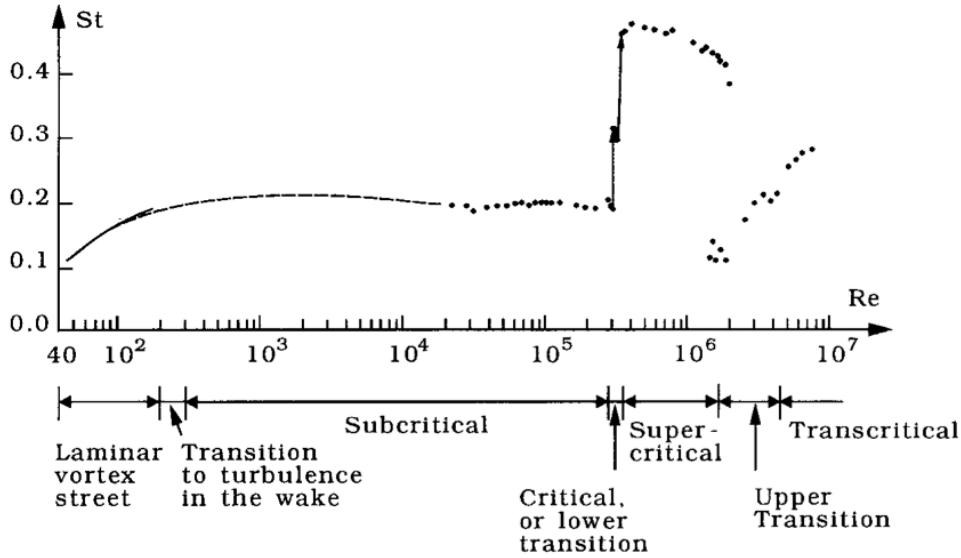


Figure 2.4: Strouhal number for a smooth circular cylinder (from Sumer & Fredsoe (2006))

2.2 Forces

2.2.1 Forces acting on a cylinder

The impact between the fluid and the structure has two main contributions; pressure and friction. The in-line, mean components of the pressure force and the friction force are denoted \bar{F}_p and \bar{F}_f , respectively. The total in-line force, the mean drag force, is given by the sum of these forces:

$$\bar{F}_D = \bar{F}_p + \bar{F}_f \quad (2.3)$$

As a result of the vortex shedding, the pressure distribution around the object will vary. This results in a cross-stream force, the lift force. Due to symmetry in the flow the mean lift force will be zero.

The vortex shedding phenomenon makes the pressure distribution dependent of time. The distribution undergoes a periodic change as the shedding process progresses. This results in a periodic variation in the force components on the cylinder. Figure 2.5 shows how the forces are changing throughout a time-series. The lift force oscillates around zero at the vortex-shedding period, T_v , while the drag force oscillates around the mean drag at $\frac{1}{2}T_v$.

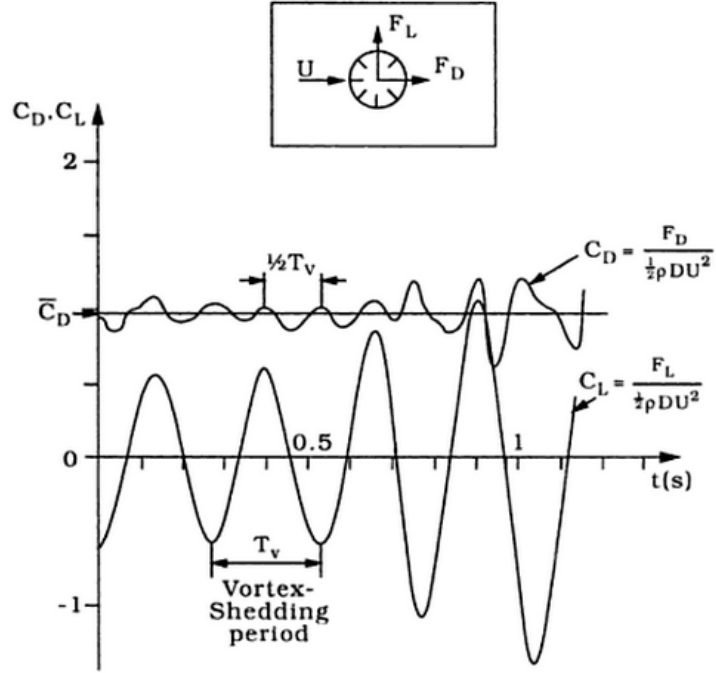


Figure 2.5: Drag and lift traces obtained from the measured pressure distributions (from Sumer & Fredsoe (2006))

2.2.2 Force coefficients

The coefficients for the instantaneous drag and lift forces are defined as follows:

$$C_D = \frac{F_D}{\frac{1}{2}\rho U_\infty^2 D}, \quad (2.4)$$

$$C_L = \frac{F_L}{\frac{1}{2}\rho U_\infty^2 D} \quad (2.5)$$

where ρ is the density of the fluid, F_D is the drag force and F_L the lift force. Figure 2.5 illustrates the coefficients for a time series.

2.2.3 Pressure distribution

For $Re \gtrsim 10^4$, the contribution of the friction drag to the total drag force is less than 2 - 3% (Sumer & Fredsoe 2006). For these cases the total mean drag can be assumed to be composed of the form drag

$$\overline{F}_D \cong \overline{F}_p \quad (2.6)$$

Figure 2.6 illustrates the measured pressure distributions for different values of Re . The pressure distribution obtained from the potential flow theory is given by

$$\bar{p} - p_0 = \frac{1}{2}\rho U_\infty^2 (1 - 4 \sin^2 \phi) \quad (2.7)$$

in which \bar{p} is the mean pressure, p_0 is the hydrostatic pressure and ϕ is the angular coordinate. There are two important distinctions between the measured pressure distribution and the potential theory; the pressure at the rear side is negative and near-to constant. The negative pressure at the rear side is due to separation. The wake region is weak compared to the outer-flow, resulting in a near-to constant value.

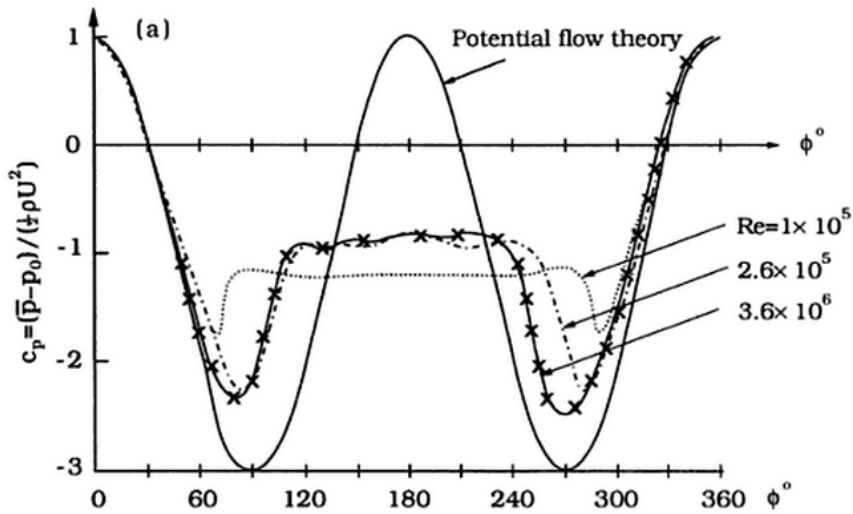


Figure 2.6: Pressure distribution at different Re numbers for a smooth cylinder (from Sumer & Fredsoe (2006))

2.2.4 Effect of cross-sectional shape on force coefficients

Changing the cross-section will change the flow topology and the behaviour of the vortex shedding process. This will influence the resulting force. While the circular cylinder is the main example of bluff bodies with rounded geometries, the rectangular cylinder, including the square section, is the main example for a sharp-edged bluff body. For cases of cross-sectional shapes with sharp edges, there are practically no Reynolds number dependence. The separation points are fixed at the sharp corners of the cross section. Therefore, no change in force coefficients is expected with change of Re for these cross-sections, in contrast to what occurs in the case of circular cross-section. Non-circular cross-sections may also be subject

to steady lift at a certain angle of attack. This is due to the asymmetry of the flow.

In the following text, the Reynolds number, the Strouhal number and the force coefficients are defined as follows

$$Re_D = \frac{U_\infty D}{\nu} \quad (2.8)$$

$$Re_B = \frac{U_\infty B}{\nu} \quad (2.9)$$

$$St = \frac{f_v D}{U_\infty} \quad (2.10)$$

$$C_D = \frac{F_D}{\frac{1}{2}\rho U_\infty^2 D} \quad (2.11)$$

$$C_L = \frac{F_L}{\frac{1}{2}\rho U_\infty^2 D} \quad (2.12)$$

B and D are shown in figure 1.2.

3 CFD

3.1 Introduction

Computational Fluid Dynamics is a numerical tool used for analysis of systems involving fluid flow, heat transfer and associated phenomena such as chemical reactions. The tool has continuously been developed since the 1960's, when the aerospace industry first started using CFD techniques in the design process. Today the technique is very powerful and is playing an increasingly important role in a wide range of industrial and non-industrial application areas. Different CFD modelling have been covered in many published works, e.g. Ferziger & Perić (2002), Versteeg & Malalasekera (2007).

All CFD procedures contain three main parts; pre-processing, a solver and post-processing.

In the pre-processing stage all input that is needed for the solver is defined. The following is determined:

- Computational domain
- Grid generation
- Selection of phenomena to be modelled
- Definition of fluid properties
- Specification of boundary conditions

The fluid problems are solved in nodes inside each cell in the grid. The number of cells in the grid is therefore directly connected to the accuracy of the solution and the calculation time. An increasing number of cells will in general result in a more accurate solution and an increased computational time.

The fluid problem is solved by the use of discretisation methods. Using discretisation methods the differential equations are approximated as a system of algebraic equations. The most used numerical solution techniques are the finite difference, the finite element, the finite volume method and spectral methods. The method with broadest applicability is the finite volume method.

The last stage is the post-processing. The solution from the solver is processed. The results might be presented through different options, e.g. plots, animations, particle tracking.

3.2 OpenFOAM

In the present study the CFD-package OpenFOAM (Open Field Operation and Manipulation) is used. OpenFOAM is a C++ library, used to solve problems in continuum mechanics. OpenFOAM is a free, open source software, mostly used to solve CFD cases. The overall structure of OpenFOAM is shown in Figure 3.1.

The minimum set of files that are required to run an OpenFOAM case are divided into three main directories; *0*, *constant* and *system*:

The *0* directory contains files describing the initial boundary conditions.

The *constant* folder contains a full description of the mesh and files specifying physical properties for the case, e.g. fluid properties and choice of turbulence model.

The *system* folder contains files for setting parameters associated with the solution procedure.

By splitting the geometry and associate fields into sub-domains and assign the sub-domains to separate processors, the applications can be run in parallel. The MPI communication protocol is used for communication between the processors.

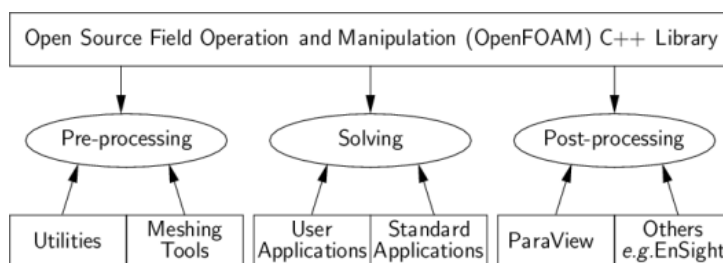


Figure 3.1: Structure of OpenFOAM (adapted from OpenFOAM Ltd. (2014))

3.3 Meshing

One of the first steps of a CFD procedure is to create a mesh. Since the differential equations governing the fluid flow are usually not possible to solve analytically, the domain has to be divided into smaller regions, or cells. The equations are then discretized (as explained later) and solved inside each cell. Continuity of the mesh is important so that approximate solutions for each element can be put together, to give a picture of the whole domain. When performing a CFD simulation, it is crucial that the boundary layers near the walls are captured properly. The grid has a significant impact on the rate of convergence, the accuracy of solution and the CPU-time of the simulation. A favourable mesh keeps the transition between the elements low, whilst keeping the total number of elements low. A poor quality grid will cause inaccurate solutions and high computational costs. The grid must satisfy certain requirements to ensure that a certain, correct solution is given. Three measurements of the quality of the mesh are the aspect ratio, the skewness and the smoothness.

There are three classes of meshes used for CFD; structured, multi-block structured and unstructured. For a structured mesh the grid can be directly transformed into a matrix, with position identified by a set of indices. For each internal grid point there is a fixed number of neighbouring grid points. In a multi-block structured grid there are two or more levels of subdivisions, e.g. a coarse level and a finer level. The unstructured grids are more often used for complex geometries. This is a more flexible type of grid as the internal grid point is not restricted to a fixed number of neighbouring grid points, and the cells are not restricted to any shape. The mesh classes are shown in figure 3.2.

3.3.1 Courant number

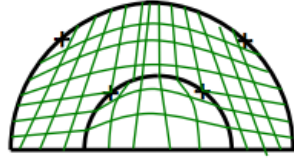
The Courant number describes the stability when solving hyperbolic partial differential equations numerically by the method of finite differences. The number indicates the convergence of an analysis. The Courant number is

$$C = U \frac{\Delta t}{\Delta x} \leq C_{max} \quad (3.1)$$

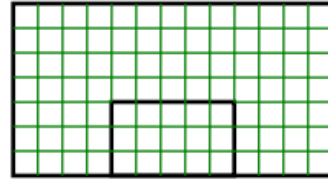
where U is the fluid velocity, Δt is the time step, Δx is the element length and C_{max} is typically equal to 1 (Ferziger & Perić 2002).

For the Courant number to be less than 1, the time step must be smaller than $\Delta x/U$.

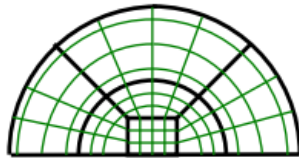
Single-block geometry



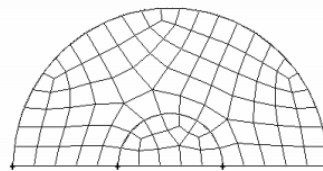
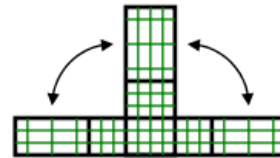
Logical representation.



Multi-block geometry



Logical representation.



Unstructured Grid

Figure 3.2: Mesh classes (adapted from Bakker (2006), with permission).

3.4 Mathematical Description

The Navier-Stokes equations are a cornerstone of fluid mechanics. The equations are describing viscous fluid flows. In most cases, even when simplifying the Navier-Stokes equations, they are not possible to be solved analytically. The solution is to use numerical methods. The Navier-Stokes equations are both the *mass equations* (the continuity equations) and the *momentum equations* (the Navier-Stokes equations). These equations are reviewed briefly in the following text.

3.4.1 Conservation of mass

Conservation of mass is widely used in fluid dynamics. The concept states that the total mass for a closed system will remain constant over time, meaning that

no mass are created or disappears. The mass-conservation equations are:

$$\frac{\partial \rho}{\partial t} + \frac{\partial \rho U_i}{\partial x_i} = 0 \quad (3.2)$$

where $i = 1, 2$, t is the time, x_i are the Cartesian coordinates and U_i are the Cartesian components of the velocity vector.

For an incompressible flow, the fluid density is constant over time in the whole system (i.e. flow in which ρ is independent both of x_i and of t). For these cases the first term of the equations disappears:

$$\frac{\partial U_i}{\partial x_i} = 0 \quad (3.3)$$

where $i = 1, 2$.

3.4.2 Conservation of momentum

The conservation of momentum comes from Newton's second law, which states that surface forces and body forces are equal to the time rate of change of momentum. The equations are:

$$\frac{\partial \rho U_i}{\partial t} + \frac{\partial \rho U_j U_i}{\partial x_j} = \frac{\partial \tau_{ij}}{\partial x_j} - \frac{\partial p}{\partial x_i} + \rho g \quad (3.4)$$

where $i=1,2$, τ_{ij} is the stress tensor, p is the static pressure and g is the gravitational acceleration.

3.5 Turbulence

Most flows that occur in practical applications are turbulent. The most defining characteristic of turbulent flows is that the fluid velocity field varies irregularly in both position and time. The fluid velocity field fluctuates in all three dimensions, making turbulence a three-dimensional phenomenon. Due to the existence of turbulence, the fluid appears to be more viscous. The flows contain a high amount of vorticity, which increases the ability of transporting and mixing the fluid.

There are many approaches to predict turbulent flows. The methods can be grouped into four main categories: the Direct Numerical Simulation (DNS) method, Large Eddy Simulation (LES) method, the Reynolds-averaged Navier-Stokes (RANS) method and hybrid methods, e.g. the Detached Eddy Simulation (DES) method. These methods are briefly introduced in the following text. For a more thorough

review the reader is referred to Pope (2000), Schlichting & Gersten (2000), Ferziger & Perić (2002).

3.5.1 DNS

The Direct Numerical Simulation is the most accurate approach to turbulence simulation. The method solves the Navier-Stokes equations for all of the motions in a turbulent flow without averaging or approximations. It therefore catches all eddy sizes, including the smallest turbulence scales. The results of a DNS contain very detailed information about the flow, but the computational cost is very high, even for low Reynolds number flows. DNS is therefore likely to play an increasingly important role in turbulence research in the near future.

3.5.2 LES

The Large Eddy Simulation solves the large scale motions of the flow while modelling the small scale motions. LES is three-dimensional, time dependent and expensive, but much less costly than DNS. A schematic representation of turbulent motion and the time dependence of a velocity component at a point is shown in figure 3.3.

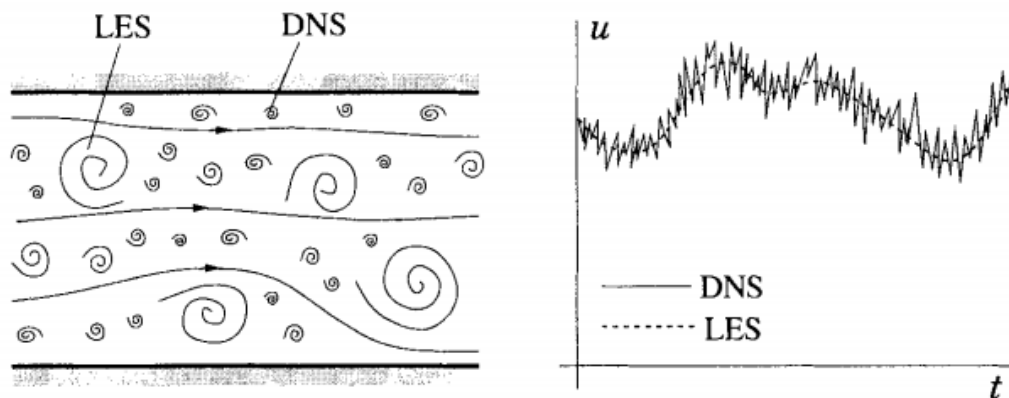


Figure 3.3: Large and small scale motions of turbulent flow (left) and the time dependence of u at a point (right) (adapted from Ferziger & Perić (2002))

3.5.3 RANS

The Reynolds-averaged Navier-Stokes equations are time averaged Navier-Stokes equations. The RANS method involves solving the RANS equations to determine the mean velocity field. The focus is on the mean values and how the turbulent

fluctuations influence these values. When time averaging the Navier-Stokes equations, additional terms determined by the turbulent fluctuations appear. Including these additional terms, more unknowns than equations appear. In order to solve the system, additional equations are required. These are model equations which model the enhanced stirring caused by turbulent eddies. This results in a great reduction of computational cost. The equations to be solved are given by:

$$\frac{\partial u_i}{\partial x_i} = 0 \quad (3.5)$$

$$\frac{\partial U_i}{\partial t} + \frac{\partial U_j U_i}{\partial x_j} = -\frac{1}{\rho} \left(\frac{\partial p}{\partial x_i} \right) + \nu \frac{\partial^2 U_i}{\partial x_j^2} - \frac{\partial \overline{u'_i u'_j}}{\partial x_j} \quad (3.6)$$

where $i, j = 1, 2$ and $\overline{u'_i u'_j}$ is the Reynolds stress component.

$$-\overline{u'_i u'_j} = \nu_T \left(\frac{\partial U_i}{\partial x_j} + \frac{\partial U_j}{\partial x_i} \right) - \frac{2}{3} k \delta_{ij} \quad (3.7)$$

where $i, j = 1, 2$, ν_t is the turbulent kinematic eddy viscosity, k is the turbulent kinetic energy and δ_{ij} is the Kronecker delta.

In the Unsteady Reynolds-averaged Navier-Stokes (URANS) method an unsteady mode, where the time averaged part of the velocity field is not constant in time, is chosen.

k- ε model

The Reynolds stresses are determined by a turbulence model. There are several turbulence models in use today. In the present study the k - ε model is used. This model is the simplest and the most widely used complete turbulence model. It is incorporated in most commercial CFD codes, and can be applied to any turbulent flow. The model belongs to the class of two-equation models.

The model adds two more transport equations, which must be solved simultaneously with the RANS equations. One equation for the turbulent kinetic energy, and one for the rate of dissipation of the turbulent kinetic energy. These variables approximate the eddy viscosity and the Reynolds stresses.

The k equation is given by:

$$\frac{\partial k}{\partial t} + \frac{\partial k U_j}{\partial x_j} = \frac{\partial}{\partial x_j} \left(\frac{\nu_T}{\sigma_k} \frac{\partial k}{\partial x_j} \right) + \nu_T \left(\frac{\partial U_i}{\partial x_j} + \frac{\partial U_j}{\partial x_i} \right) \frac{\partial U_i}{\partial x_j} - \varepsilon \quad (3.8)$$

where $i, j = 1, 2$, σ_k is the turbulent Prandtl number for kinetic energy and ε is the rate of dissipation of turbulent kinetic energy.

The standard model equation for ε is:

$$\frac{\partial \varepsilon}{\partial t} + \frac{\partial \varepsilon U_j}{\partial x_j} = \frac{\partial}{\partial x_j} \left(\frac{\nu_T}{\sigma_\varepsilon} \frac{\partial \varepsilon}{\partial x_j} \right) + C_{\varepsilon_1} \frac{\varepsilon}{k} \nu_T \left(\frac{\partial U_i}{\partial x_j} + \frac{\partial U_j}{\partial x_i} \right) \frac{\partial U_i}{\partial x_j} - C_{\varepsilon_2} \frac{\varepsilon^2}{k} \quad (3.9)$$

where $i, j = 1, 2$, σ_ε is the turbulent Prandtl number for dissipation, C_{ε_1} and C_{ε_2} are constants in the model equation for ε .

The standard values of all the model constants are according to recommendations from Launder & Sharma (1974):

$$C_\mu = 0.09, C_{\varepsilon_1} = 1.44, C_{\varepsilon_2} = 1.92, \sigma_k = 1.0, \sigma_\varepsilon = 1.3.$$

3.5.4 DES

Detached eddy simulation is a hybrid method combining the RANS and LES approaches. DES offers RANS in the regions near solid boundaries and LES after massive separation (Spalart et al. 1997). This way the method uses turbulence models near walls, avoiding the need for a high grid resolution, while using the LES method in the outer region. As a result, the computational cost demanded by the LES method is reduced.

3.5.5 Law of the wall

The presence of a wall has a large influence of the flow behaviour and structure of a turbulent flow. Far from the wall the inertial forces are dominating. Close to the wall the flow is influenced by viscous effects and does not depend on the free stream parameters. The mean flow velocity only depends on the distance from the wall - y , fluid density - ρ , dynamic viscosity of the fluid - μ and the wall shear stress - τ_w . The law of the wall explains the relationship between these parameters:

$$u^+ = \frac{U}{u_\tau} = f \left(\frac{\rho u_\tau y}{\mu} \right) = f(y^+) \quad (3.10)$$

u^+ is the dimensionless velocity, $u_\tau = \sqrt{\frac{\tau_w}{\rho}}$ is the friction velocity and y^+ is the dimensionless distance from the wall.

At the solid surface the fluid is stationary. For the fluid adjacent to the wall,

the relationship between velocity and distance from the wall is linear. The linear relationship is only valid for an extremely thin layer, the viscous sub-layer ($y^+ < 5$). For this layer the law of the wall can be simplified to

$$u^+ = y^+ \quad (3.11)$$

In the log-law layer ($30 < y^+ < 500$) outside the viscous sub-layer both the viscous and the turbulent effects are important. The shear stress varies slowly with distance from the wall and is assumed to be equal to the wall shear stress. The relationship between the wall velocity and the distance from the wall is derived in the log-law equation

$$u^+ = \frac{1}{\kappa} \ln(Ey^+) \quad (3.12)$$

where κ is von Karmans constant and E is a constant. For turbulent flow past smooth walls $\kappa = 0.41$ and $E = 9.8$ (OpenFOAM Ltd. 2014).

Figure 3.4 illustrates the close agreement between theoretical equations and experimental data.

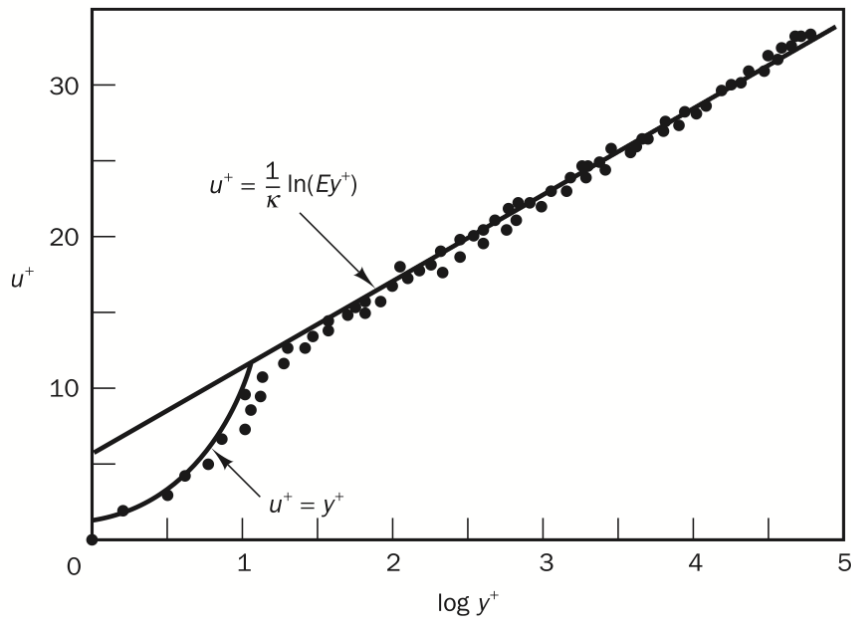


Figure 3.4: Velocity distribution near a solid wall (from Versteeg & Malalasekera (2007))



4 Numerical set-up

The main focus of this thesis was to perform simulations of flows around rectangular cylinders with various aspect ratios. In order to perform these simulations the numerical set-up for the solver must be defined. This involves to determine the computational domain, build grids, set boundary conditions and to set up the solver. These steps are discussed in the present chapter.

4.1 Domain

The size of the computational domain is of great importance. Choosing a poor computational domain might give inaccurate results. A too small domain is not able to capture the whole velocity field that is influenced by the cylinder, and therefore important effects might get neglected.

The dimensions of the rectangular cylinders are shown in Figure 1.2. The origin is placed in the center of the cylinder. The inlet is placed $10D$ upstream of the origin and the outlet $30D$ downstream. The top and bottom boundaries are placed $10D$ from the centreline. Hence, the total size of the domain is $40D \times 20D$. The square cylinder with surrounding domain is shown in figure 4.1. The same domain is used for all aspect ratios. The size of the domain is, according to Ong (2012), of sufficient size to eliminate the far field effects on the flow upstream and downstream of a 5:1 rectangular cylinder at $Re_D = 1 \times 10^5 - 4 \times 10^5$.

Mannini et al. (2011) maintained that the 3D DES approach gave an improved quality of the simulations with respect to 2D and 3D URANS methods, but that the requirements of fine three-dimensional meshes, small time steps and reasonable statistical convergence of the computed flow field made the approach quite expensive for the simulation of bluff body flows. Bruno et al. (2010) used LES to evaluate whether 3D flow features exist around a nominally 2D rectangular cylinder. They reported that even though the 3D flow features are not negligible, the main phenomena which drive the aerodynamic forces remain 2D. Hence, it is valid

that 2D simulations are carried out in the present study.

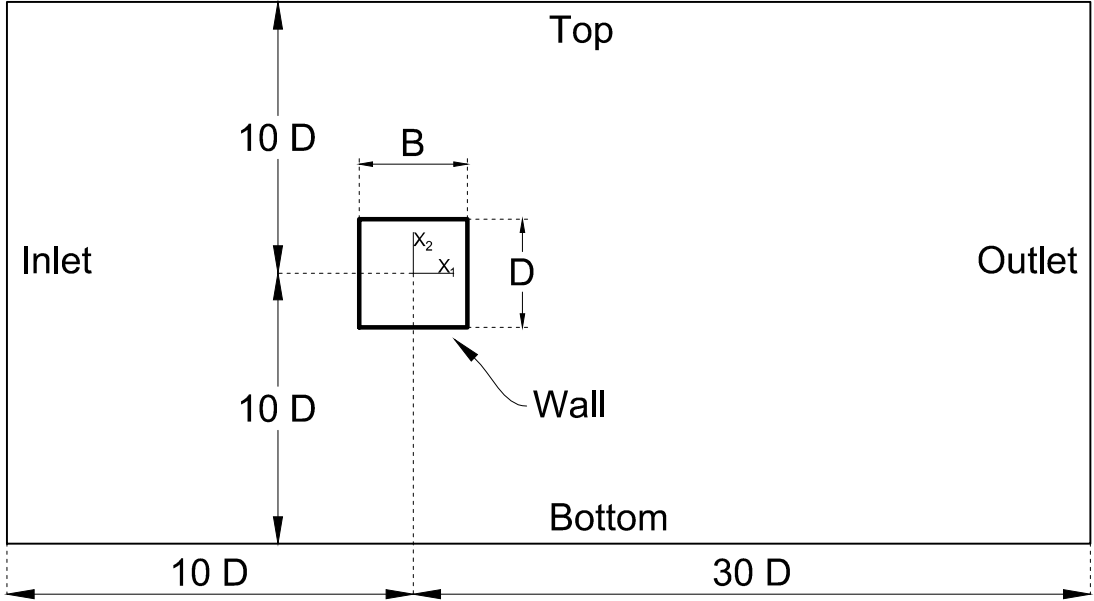


Figure 4.1: Computational domain (the cylinder is not to scale)

4.2 Boundary Conditions

When solving the RANS equations, appropriate initial conditions and boundary conditions need to be applied. The domain in the present study is divided into 6 boundaries; “*inlet*”, “*outlet*”, “*wall*”, “*top*”, “*bottom*” and “*front and back*”. The location of the boundaries are shown in figure 4.1. The *front and back* boundaries are the X_1X_2 -planes of the domain.

Velocities and pressure

The boundary condition “patch” is used for the *inlet*. This condition contains no geometrical or topological information about the mesh. Uniform flow is specified with $U_1 = U_\infty$ and $U_2 = 0$. The pressure is set to “zeroGradient”.

Also for the *outlet*, the “patch” boundary condition is used. The velocities are set to “zeroGradient”, while the pressure is set to zero.

The *wall* has a “wall” boundary, which means that there will be no flow through

the surface of the cylinder and the no-slip condition shall be fulfilled. The velocities are set to zero along the cylinder, while the pressure is set to zeroGradient.

For the *top* and *bottom* boundaries, velocities and pressure are set to “symmetry-Plane”. This condition states that there will only be parallel flow to the boundaries (no flow across the boundaries).

For the *front and back* boundary condition, the velocities and the pressure are set to “empty”, which makes the problem two-dimensional.

***k*- ε model**

When using the *k*- ε model, *k*, ε and ν_T must to be defined along boundaries. These boundaries are as follows:

At the inlet, the free stream inlet turbulence values for kinetic energy are calculated using

$$k = \frac{3}{2}(I_u U_\infty)^2 \quad (4.1)$$

and the turbulent dissipation

$$\varepsilon = \frac{C_\mu k^{3/2}}{0.1L} \quad (4.2)$$

where the turbulence intensity, $I_u = \frac{U_1}{U_\infty}$, is set to 0.8% and the non-dimensional turbulent length scale (L/D) is 0.0045 (Ong 2012).

On the cylinder, the near-wall conditions are applied as:

$$k = \frac{u_\tau^2}{\sqrt{C_\mu}}$$

$$\varepsilon = C_\mu^{3/4} \frac{k^{3/2}}{\kappa h_p} \quad (4.3)$$

where h_p is the normal distance between the first node and the wall and $\kappa = 0.41$. u^+ is obtained using the log law equation (see equation 3.12). The equation is applicable for $y^+ \geq 30$, where $y^+ = h_p u_\tau / \nu$.

The turbulent viscosity is specified as:

$$\nu_t = C_\mu \frac{k^2}{\varepsilon} \quad (4.4)$$

Table 4.1 shows the resulting boundary values for k , ε and ν_t for the wall and inlet boundaries. At the remaining boundaries k , ε and ν_t are set to zero.

Table 4.1: Boundary conditions for k , ε and ν_t

B/D	Boundary	k	ε	ν_t
1	wall	0,001966	0,004991	6.97×10^{-5}
2	wall	0,001053	0,001523	6.56×10^{-5}
3	wall	0,001189	0,001826	6.97×10^{-5}
4	wall	0,001333	0,002449	6.56×10^{-5}
5	wall	0,001783	0,003770	7.585×10^{-5}
1, 2, 3, 4, 5	inlet	0,000096	0,0001881	4.409×10^{-6}

4.3 Mesh

Creating a mesh for high Reynold number flows around sharp edged objects is a detailed and sensitive task. The solution is sensitive to areas with high pressure gradients. It is therefore important to create a mesh with fine cells in these areas. The high pressure gradients are often observed close to walls and especially close to the corners of the objects. In the areas where the pressure gradients are smaller, coarser cells can be used to keep the total number of cells as low as possible without affecting the solution.

All grids for the present simulations are block-structured, containing 29 blocks. The block-topology used for building the mesh around a square cylinder is shown in figure 4.2. One of the corresponding meshes built by this topology (as later referred to as A1M1) is shown in figure 4.3. In order to control the mesh, three areas are created; a boundary layer, a near-field area and a far field area. The boundary layer contains the finest elements. The thickness of the layer is chosen to be $0.2D$. The near-field is defined by a circle centred in the origin with a radius of $6D$. In the far field area the coarsest elements are present. The number of elements, element size on the ends and/or growth ratio is specified on each edge. The normal distance between the first node and the wall is different for each aspect ratios, being in the range of $h_p = 0.0065D - 0.009D$. The growth ratios on the edges are in the range of 0 – 10%.

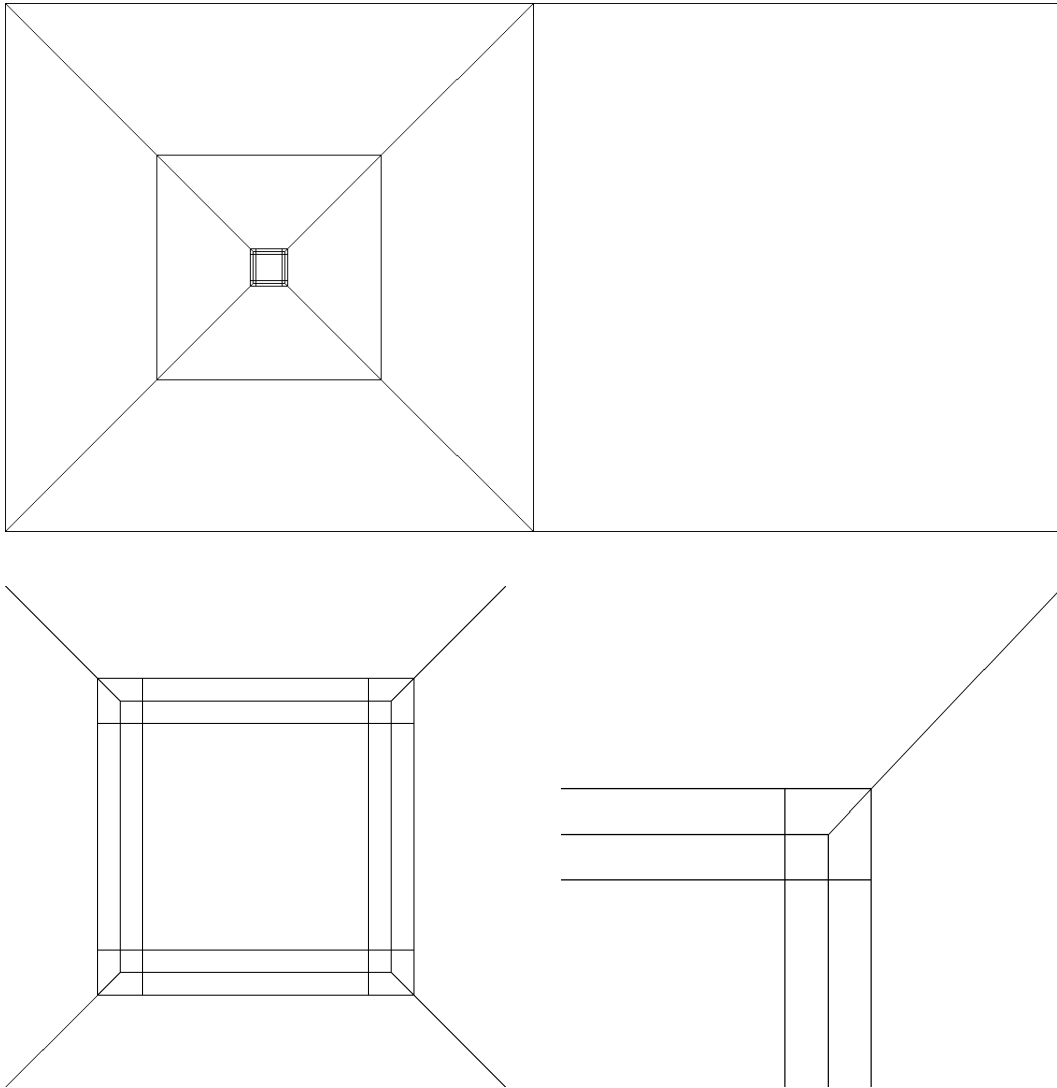


Figure 4.2: The block-topology used for building the mesh around a square cylinder

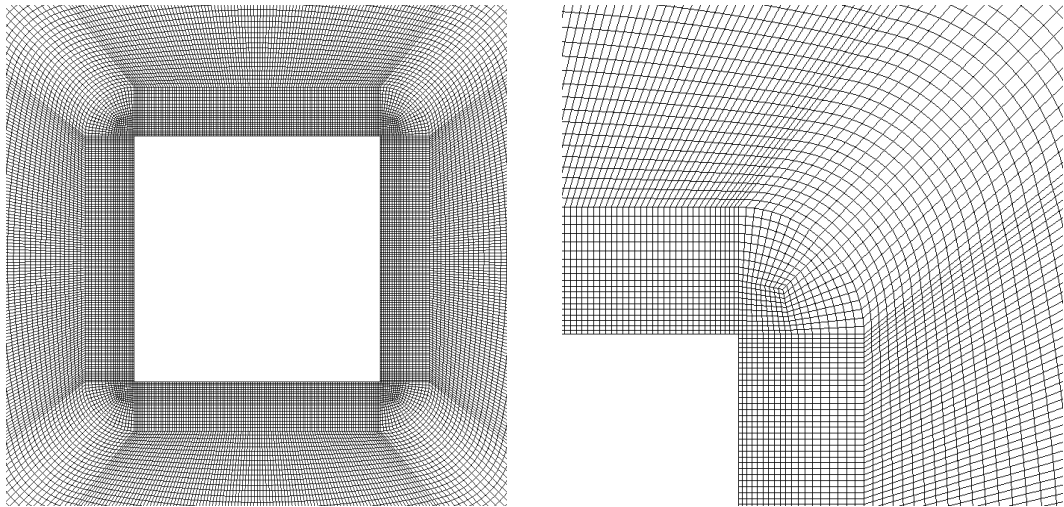
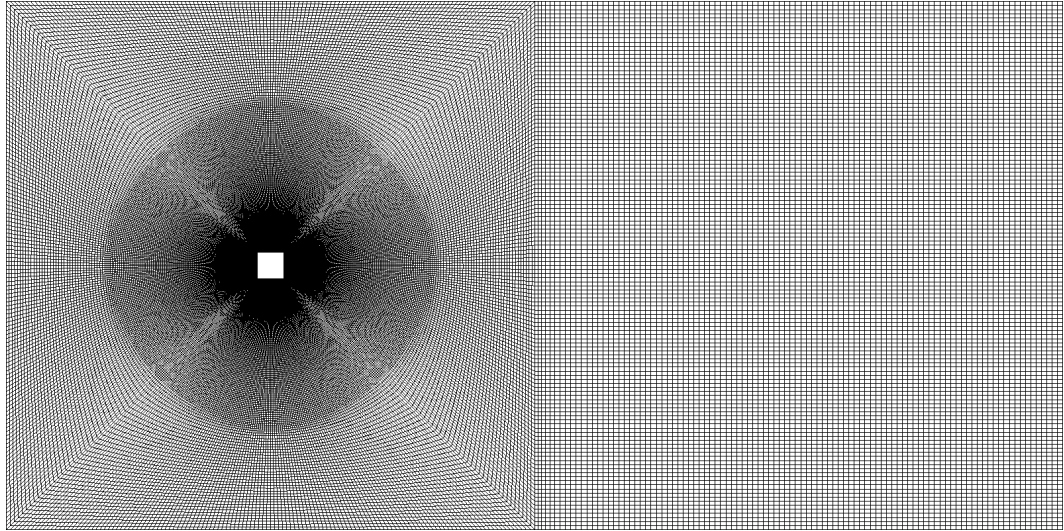


Figure 4.3: The mesh around a square cylinder

4.4 OpenFOAM

OpenFOAM has a wide range of standard solvers. In the present study the pisoFOAM solver is used. pisoFOAM is a transient solver for incompressible flow (OpenFOAM Ltd. 2014). The solver uses the PISO (Pressure Implicit with Splitting of Operators) scheme. The Reynolds-Averaged Simulation (RAS) flow model, which uses the RANS/URANS methods, is chosen. The high Reynolds number $k-\varepsilon$ turbulence model kEpsilon has been implemented. For wall functions the epsilon-WallFunction and kqRwallFunction are used. These functions uses the log-law as described in section 3.5.5.

OpenFOAM also offers a wide range of numerical schemes for different terms in the equations. A description of these schemes is found in the OpenFOAM User Guide (section 4.4, OpenFOAM Ltd. (2014)). The settings are implemented in the file fvSchemes in the *system* directory. The schemes for gradient, Laplacian and divergence are Gauss linear, Gauss linear corrected and Gauss linear schemes, respectively. All these schemes are in second order. The CrankNicholson scheme is used for the time integration.

The settings for solvers presented in the OpenFOAM User Guide are used in the present study (section 4.5, OpenFOAM Ltd. (2014)). The settings are implemented in the file fvSolution in the *system* directory. The solver for p is preconditioned conjugate gradient (PCG) with a Diagonal incomplete-Cholesky (DIC) preconditioner. A preconditioned conjugate gradient (PBiCG) solver with a Diagonal incomplete-LU preconditioner is used for U, k, ε , $\overline{u'_i u'_j}$ and ν_t .

The simulations are run in parallel on distributed processors using the “simple” method. This is done by a simple domain decomposition, where the mesh is split into sub-domains by direction.

Details of the numerical set-up can be found in appendix A.

4.5 High Performance Computing - Vilje

The simulations are run on the supercomputer *Vilje*. The computer is produced by SGI and runs on SUSE Linux. The system is acquired by NTNU together with met.no and UNINETT Sigma. The system is used at NTNU for research in a broad range of topics. It is also used for numerical weather predictions by met.no.

Some details about Vilje are listed below:

- Number of nodes: 1404
- Processors per node: 2 eight-core processors
- Processor speed: 2.6 GHz
- Memory: 2 GB per core

Each simulation in the present study is run with 2 nodes with a total number of 32 cores. A total of 34095 core hours have been used.

5 Results and discussion

Numerical simulations of flow around rectangular cylinders with aspect ratios $B/D = \{1, 2, 3, 4, 5\}$ have been performed. A Reynolds number of $Re_D = 2 \times 10^5$ has been chosen for all simulations. The average value of the dimensionless distance from the first node to the wall, y^+ , was in the present study in the range of $30 < y^+ < 40$, to fulfil the log-law requirements. Essential hydrodynamic quantities, such as the mean drag coefficient $\overline{C_D}$, the root mean square (RMS) value of the lift coefficient C_{Lrms} , the Strouhal number, the pressure distribution around the cylinder and the mean streamwise velocity profiles have been predicted. $\overline{C_D}$, C_{Lrms} and St are defined by the cylinder height, D .

The first simulations of each aspect ratio, 1, 2, 3, 4 and 5, are named A1M1, A2M1, A3M1, A4M1 and A5M1, respectively. The boundary conditions calculated in the finale time-step of these simulations are used as initial boundary conditions for the remaining cases. This ensures a quick convergence towards a stable result. All simulations are run for a duration of $200D/U_\infty$ after being fully developed.

5.1 Validation of the numerical model

The 5:1 rectangular cylinder has been used for the purpose of validating the applicability of the 2D URANS with the standard high Reynolds number $k-\varepsilon$ turbulence model. The rectangular cylinder was chosen as a benchmark study in 2008 (Bartoli et al. 2008). This has resulted in a large number of realizations of the flow configuration, both numerical and experimental, which gives the opportunity to verify the model used in the present study.

5.1.1 Results

The time history of force coefficients obtained in the case A5M2 is plotted in figure 5.1. The plot is from the time interval $200 \leq tU_\infty/D \leq 300$, where the vortex shedding process is fully developed. As seen from the plot a stable result is obtained without any disturbance from the turbulence. The smooth curves are

a result of the averaging in the URANS method. The lift coefficient is fluctuating about a mean value of zero, with significantly larger amplitude than the amplitude of the fluctuating drag coefficient. The frequency of the fluctuations found for the drag coefficient is twice the frequency of the fluctuations found for the lift coefficient.

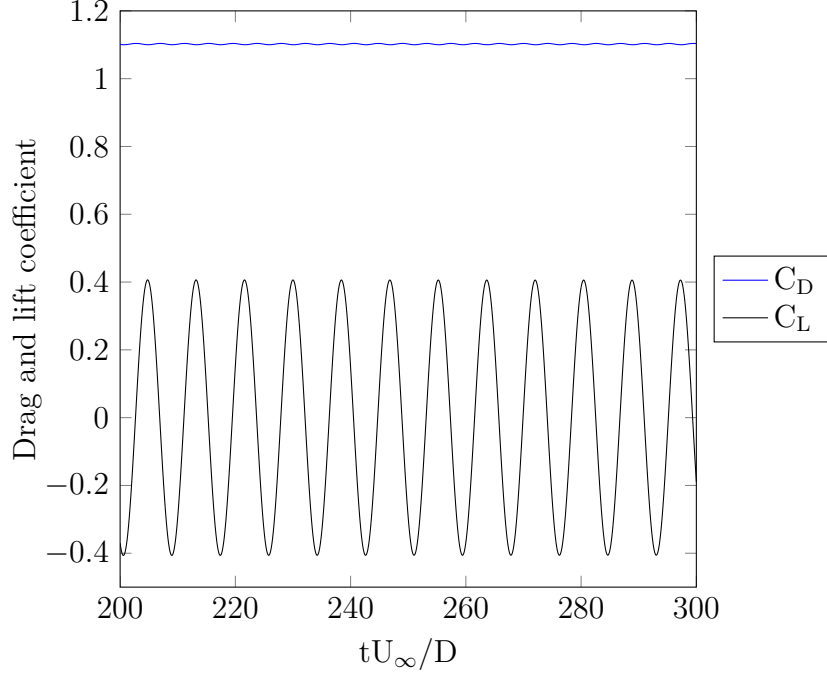


Figure 5.1: Time history of force coefficients from case A5M1

The results from the simulations are posted in table 5.1. A grid convergence study has been performed with 4 mesh configurations. The total number of elements are ranging from 109332 to 220956. The simulations are run with an average value of $y^+ = 32$ and an average Courant number of $C = 0.03$ and maximum value of $C_{max} \approx 0.5$. As seen from table 5.1 and figure 5.2 there is a convergence for the mean drag coefficient and the root mean square of the lift coefficient. The relative change is calculated by taking the variation of hydrodynamic results between two consecutive meshes or time steps with respect to the median of them. The relative changes found between case A5M3 (186376 elements) and case A5M4 (220856 elements) are less than 0.019% for \overline{C}_D and less than 1.30% for C_{Lrms} . The Strouhal number is unchanged in the simulations.

A time step (Δt) of $0.002D/U_\infty$ is used for the grid convergence study. A time step test is also carried out using the mesh from case A5M3. The results of \overline{C}_D

and C_{Lrms} do not change significantly as the time step is changed to $0.0015D/U_\infty$ (case A5M5) and $0.0025D/U_\infty$ (case A5M6). The relative changes found are less than 0.073% for \overline{C}_D and 0.80% for C_{Lrms} . The Strouhal number remains identical for the cases. Hence case A5M3 with $\Delta t = 0.002D/U_\infty$ is concluded to give a sufficient numerical accuracy.

Table 5.1: Mesh and time convergence study of hydrodynamic quantities for rectangular cylinder with aspect ratio 5

Case	Elements	Δt	\overline{C}_D	C_{Lrms}	St
A5M1	109332	0.002	1.1040	0.3070	0.1221
A5M2	143852	0.002	1.1020	0.2870	0.1221
A5M3	186376	0.002	1.1008	0.2760	0.1221
A5M4	220856	0.002	1.1010	0.2796	0.1221
A5M5	186376	0.0015	1.1016	0.2782	0.1221
A5M6	186376	0.0025	1.1004	0.2757	0.1221

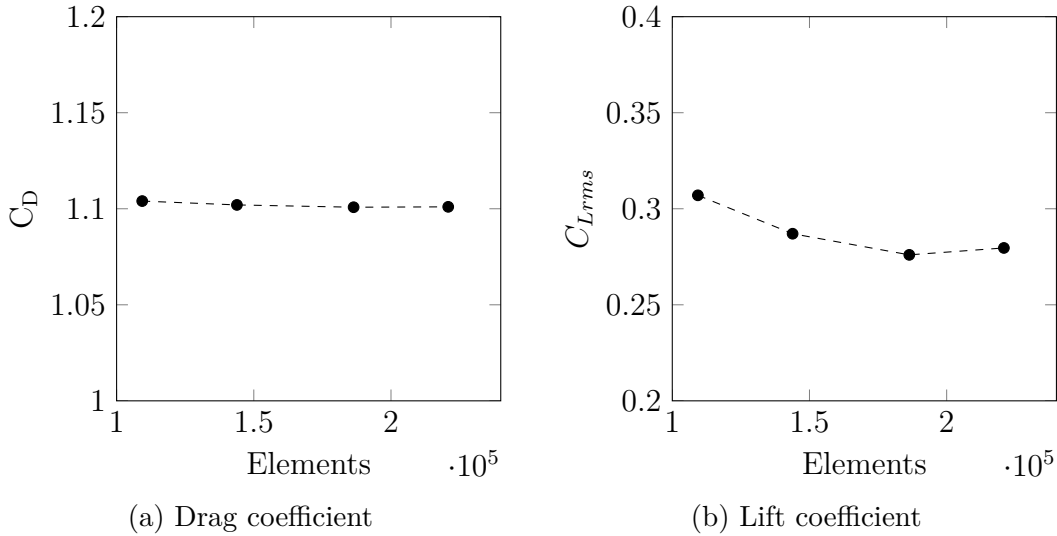


Figure 5.2: Mesh convergence of drag and lift coefficient.

Table 5.2 shows the hydrodynamical quantities obtained from the present simulations, published experiments (Schewe (2006, 2009), Bartoli et al. (2011)) and numerical results (Ong (2012), Bruno et al. (2010), Mannini et al. (2011)). Bruno et al. (2014) created an ensemble average over all available data, which is also found

in table 5.2. The hydrodynamic quantities calculated from the present study are in good agreement with published results. The \overline{C}_D is predicted slightly above the published experimental and numerical values at same Reynolds number. The C_{Lrms} and the Strouhal number show a good agreement.

Table 5.2: Hydrodynamic quantities for rectangular cylinder with aspect ratio 5

Source/Author	Method	Re_D	\overline{C}_D	C_{Lrms}	St
Present study	2D k- ε	2×10^5	1.1008	0.2760	0.1221
Schewe (2006, 2009)	Exp.	2×10^5	0.9612	~ 0.4	0.111
Bartoli et al. (2011)	Exp.	8×10^4	-	-	0.12
Ong (2012)	2D k- ε	2×10^5	0.9765	0.1704	0.1221
Bruno et al. (2010)	3D LES	4×10^4	1.0423	0.7222	0.1105
Mannini et al. (2011)	3D DES	2.64×10^4	0.968-1.071	0.42-1.075	0.094-0.102
Ensemble average ¹			1.074	0.65	0.109

¹ Data obtained from Bruno et al. (2014)

5.1.2 Pressure

The average pressure coefficient over the cylinder surface, \overline{C}_p , is shown in figure 5.3. The definition of S/D is shown in figure 1.2. Only half of the cylinder surface is plotted due to symmetry. The coefficient is found by the use of equation 5.1.

$$\overline{C}_p = \frac{\overline{p} - p_0}{\frac{1}{2}\rho U_\infty^2} \quad (5.1)$$

where p_0 is the inlet pressure.

From the figure it is seen that the pressure coefficient is equal to 1 in the stagnation point, where the velocity is zero. As the fluid particles follow the surface of the cylinder towards the leading corner, the particles gets accelerated and the pressure coefficient drops rapidly towards a negative value close to -1. From the leading corner to the trailing corner the velocity is decreasing and though the pressure coefficient increases towards a value of about -0.3 . A small drop occurs at the trailing corner before the \overline{C}_p increases towards a value of -0.3277 .

The results are compared with the numerical results from Ong (2012) at $Re_D = 4 \times 10^5$ and experimental data from Galli (2005) at $Re_D = 4.2 \times 10^4$ (data obtained from Mannini et al. (2011)) and Matsumoto (2005) (data obtained from Mannini

et al. (2010)) at $Re_D = 4 \times 10^4$. There is a good agreement between the present predicted C_p and the mean pressure coefficient reported by Ong (2012). Both distributions are found using the high Reynolds number $k - \varepsilon$ model. The predicted coefficient is also in relatively good agreement with the experimental data from Galli (2005) and Matsumoto (2005), but a deviation is found for $0.5 < S/B < 5.5$. There are no experimental data for the mean pressure coefficient around a rectangular cylinder for $Re_D = 2 \times 10^5$ known to the author. As Ong (2012) concluded, this might be due to the effect of Re_D , which requires more measurements of $\overline{C_p}$ to validate the model.

The mean base pressure coefficient, C_{pb} , is found to be $C_{pb} = -0.3277$. The present predicted C_{pb} is in good agreement with the measured base pressure found by Schewe (2006) at $Re_D = 2 \times 10^5$, which was found to be $C_{pb} = -0.3079$.

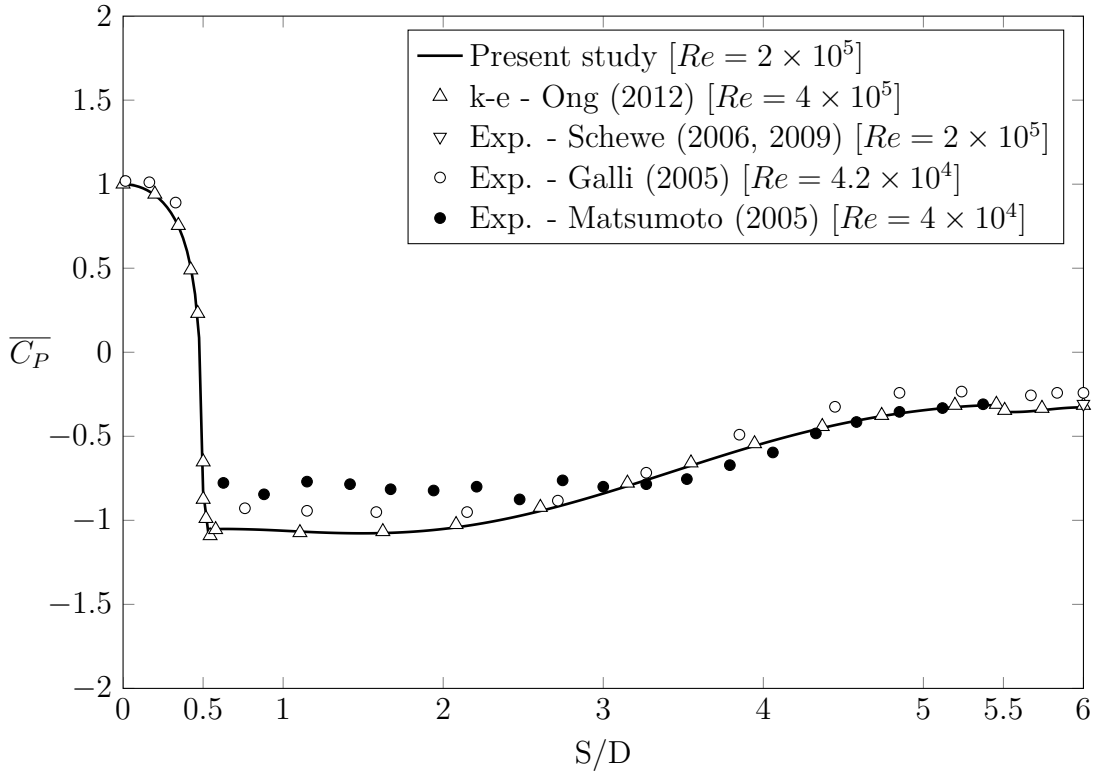


Figure 5.3: Time-averaged pressure distributions on the surfaces of the 5:1 rectangular cylinder

5.1.3 Velocity distribution

Figure 5.4 shows the mean streamwise velocity distribution along the centreline of the cylinder. The length of the mean recirculation region (where the mean velocity $\bar{U} < 0$) is found to be $3.45D$. However, there are no available published experimental nor numerical results for the validation of the mean streamwise velocity distribution along the center line.

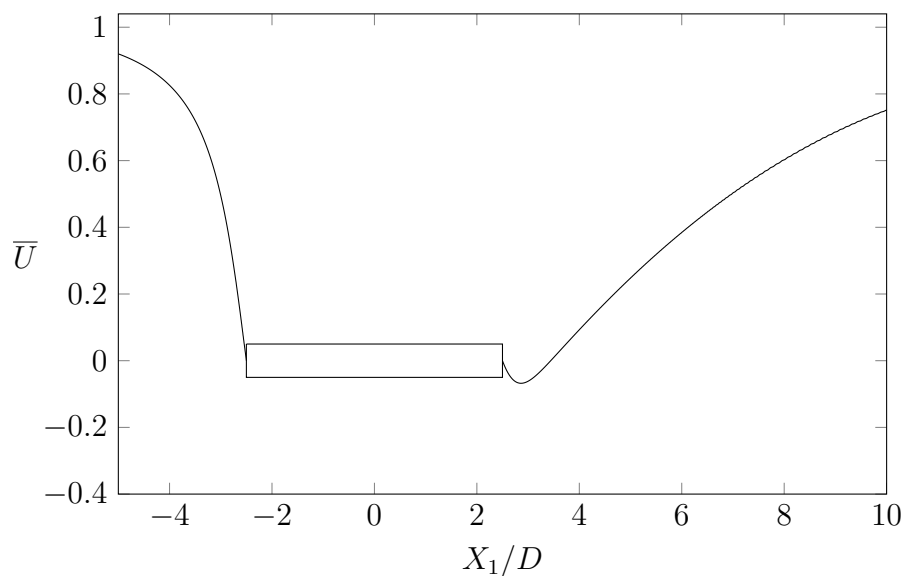
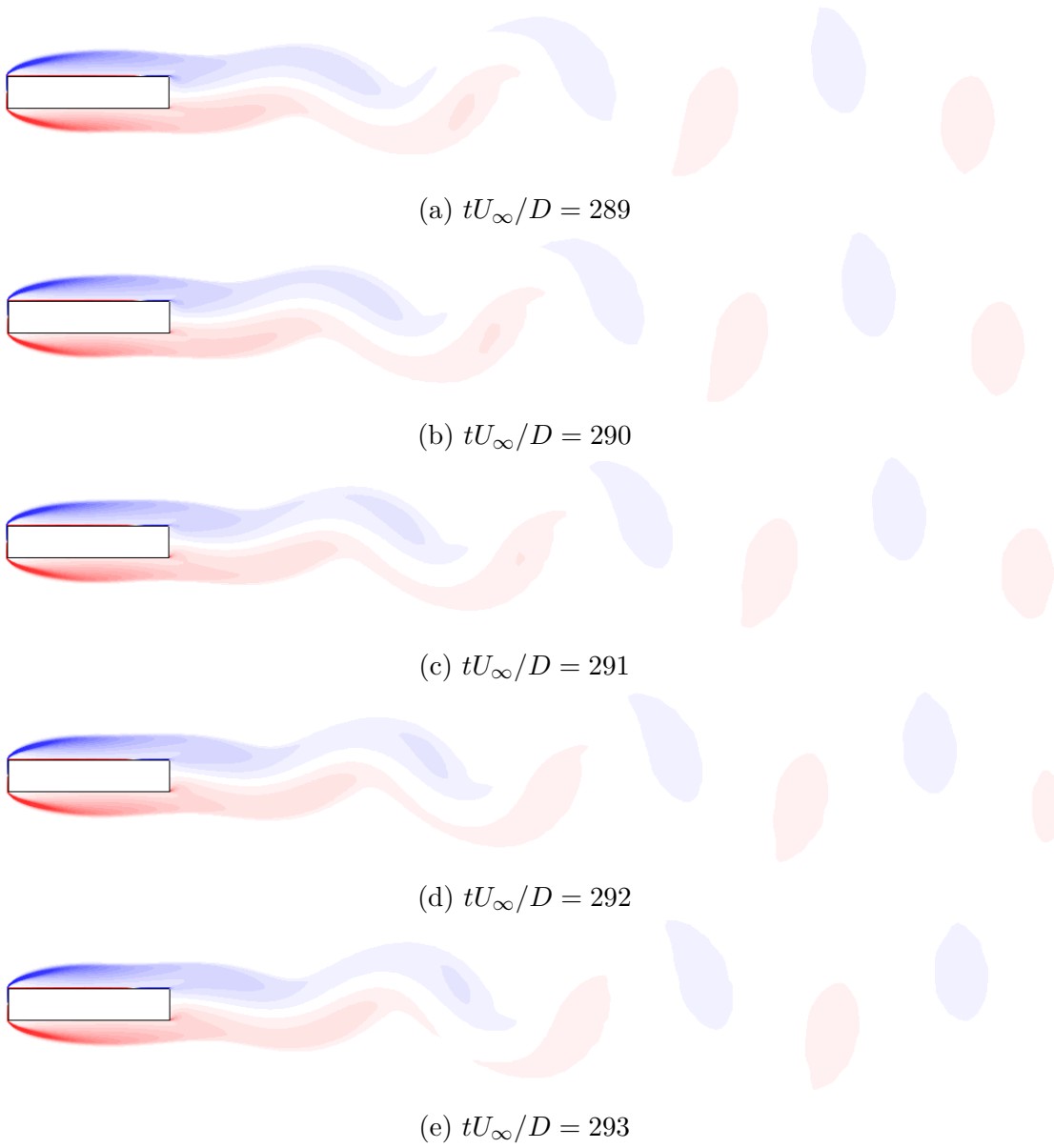


Figure 5.4: Mean streamwise velocity distribution along the centreline of the 5:1 rectangular cylinder

5.1.4 Vorticity contours

The vortex shedding period for the cylinder is found to be $T_v = 8.19D/U_\infty$. The vorticity contours from a near to full vortex shedding period of case A5M3 is shown in figure 5.5.



This figure continue on the next page

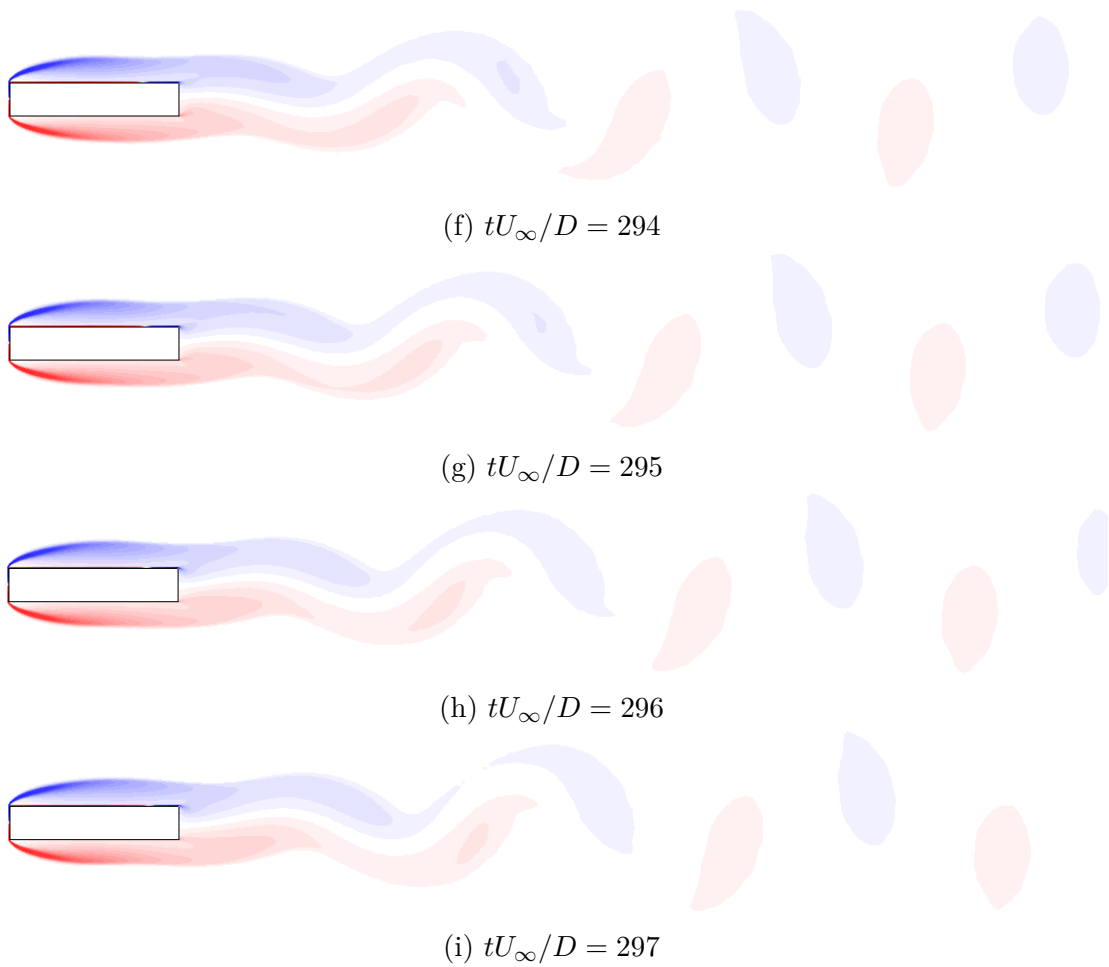


Figure 5.5: Vorticity contours from a near to full vortex shedding period of the 5:1 rectangular cylinder

5.1.5 Conclusion

The hydrodynamic quantities calculated from the present study are in good agreement with published results. The average pressure coefficient over the cylinder surface is in relatively good agreement, but small deviations are found. Overall, it appears that the present numerical model is capable of predicting the flow around the rectangular cylinder with $B/D = 5$ in both quantitative and qualitative manners.

5.2 Results

Grid convergence studies and time step tests have been performed for rectangular cylinders with aspect ratio 1, 2, 3, 4 and 5. The hydrodynamic quantities calculated in the simulations are shown in table 5.3. The first 4 cases of each aspect ratio are performing the grid convergence studies (e.g. case A1M1, A1M2, A1M3, A1M4 for aspect ratio 1) using a time step of $0.002D/U_\infty$. The total number of elements in the meshes are ranging from 71804 elements in case A2M1 to 233472 elements in case A4M4. The grid convergence studies are performed by increasing the total number of elements of a case by approximately 20 – 30%. The last two cases for each aspect ratio are testing the accuracy of the time step. The time steps $0.0015D/U_\infty$ and $0.0025D/U_\infty$ are used for the tests (e.g. case A1M5 and A1M6 for aspect ratio $B/D = 1$).

The quantities are converging as the mesh gets refined. The relative changes between the cases are calculated and presented in the table (under the “%”-symbols). The relative change is calculated by taking the variation of hydrodynamic results between two consecutive meshes or time steps with respect to the median of them. The relative changes are throughout the study higher for C_{Lrms} than for \overline{C}_D . The fluctuations of the lift coefficient are very sensitive to the complex dynamics of the flow along the cylinder breadth. For this reason the stronger parameter dependency is seen for the RMS value of the lift coefficient.

An aspect ratio dependency is apparent for all of the hydrodynamical quantities studied. The drag coefficient is close to halved as the aspect ratio is increased from $B/D = 1$ to $B/D = 5$. The RMS value of the lift coefficients are in the range of 0 - 1.4, while the Strouhal numbers are mainly alternating between 0.1221 and 0.1373. Reasons for the behaviour of the hydrodynamic quantities will be elaborated in the following text.

For $B/D = 1, 4$ and 5 the relative changes in the hydrodynamic quantities are less than 2% between the third and fourth case. For the rectangular cylinders with aspect ratio 2 and 3, the RMS value of the lift coefficient yields a significantly smaller value. The largest relative changes are therefore observed for these cases. The relative changes in the RMS values of the lift coefficients between third and fourth cases are 3.43% for $B/D = 2$ and 7.23% for $B/D = 3$. The differences in these cases are in the same order as the differences between the third and fourth case for the remaining aspect ratios. Hence, these values are considered to give acceptable numerical accuracy.

The Strouhal number stays unchanged for the grid convergence study for all aspect

ratios. It also stays unchanged for the time step tests performed for aspect ratio 2 and 5. A time step dependency is seen for aspect ratio $B/D = 1, 3$ and 4. For aspect ratio 3 a change in the Strouhal number is observed when increasing the time step. It stays unchanged as the time step is decreased. The Strouhal number behaviour for $B/D = 1$ and 4 is identical. The number increases both when the time step is increased to $0.0025D/U_\infty$ and when it is decreased to $0.0015D/U_\infty$. This might indicate that a fluctuating solution dependent of the time step is present. It is concluded that a time step of $0.002D/U_\infty$ is seen to be sufficient for all aspect ratios.

Overall, it is concluded that the present simulations can provide satisfactory spatial and time resolutions for all the five aspect ratios at $Re_D = 2 \times 10^5$. All results presented in the following sections are obtained from the cases labelled by “*” in table 5.3.

5.3 Effect of aspect ratio

5.3.1 Forces and Strouhal number

The figures 5.6, 5.7 and 5.8 show the variations of the mean drag coefficient, the RMS value of the lift coefficient and the Strouhal number according to the aspect ratio. Both experimental and numerical results are presented for comparison. Published results with flows at $Re_D = 2 \times 10^5$ are only found for aspect ratio 5. The data are color labelled with a dependence of the Reynolds number. Black markers in figure 5.6, 5.7 and 5.8 are used for data found at $Re = 2 \times 10^5$. Blue markers are used for results with flows at $4 \times 10^4 < Re_D < 2 \times 10^5$, while red markers are used for data found using flows with $Re_D \leq 4 \times 10^4$. The corresponding references are labelled to the right of the plots. The data found using a Reynolds number $Re_D < 2 \times 10^5$ will be used as indicators of the behaviour of the hydrodynamic quantities.

Mean drag coefficient

The largest values of the mean drag coefficient are found for aspect ratio 1. As the aspect ratio increases, both the mean drag coefficient and the difference in drag force between two aspect ratios decreases. This behaviour is also seen in the reference data in figure 5.6.

As mentioned in section 2.3.3, for $Re > 10^4$ the total mean drag force on a circular cylinder can be assumed to be caused by the pressure force. The same assumption can be made for rectangular cylinders with aspect ratios from 1 to

Table 5.3: Results from grid convergence study and time step test for rectangular cylinders with aspect ratio 1, 2, 3, 4 and 5

B/D	Case	Elements	Δt	\bar{C}_D	%	C_{Lrms}	%	St
1	A1M1	95280	0.002	2.0972		1.4008		0.1373
1	A1M2	126928	0.002	2.0971	0.005	1.3986	0.16	0.1373
1	A1M3*	155300	0.002	2.0984	0.062	1.4018	0.23	0.1373
1	A1M4	182980	0.002	2.0993	0.043	1.4140	0.87	0.1373
1	A1M5	155300	0.0015	2.0991	0.033	1.3985	0.24	0.1424
1	A1M6	155300	0.0025	2.0974	0.048	1.4060	0.30	0.1465
2	A2M1	71804	0.002	1.4872		0.0426		0.1221
2	A2M2	103696	0.002	1.4946	0.496	0.0459	7.46	0.1221
2	A2M3*	144674	0.002	1.4935	0.074	0.0445	3.10	0.1221
2	A2M4	183274	0.002	1.4916	0.127	0.0430	3.43	0.1221
2	A2M5	144674	0.0015	1.4934	0.007	0.0444	0.22	0.1221
2	A2M6	144674	0.0025	1.4935	0	0.0448	0.67	0.1221
3	A3M1	109616	0.002	1.3194		0.0507		0.1221
3	A3M2	141412	0.002	1.3213	0.144	0.0447	12.6	0.1221
3	A3M3*	179884	0.002	1.3201	0.091	0.0444	0.67	0.1221
3	A3M4	231552	0.002	1.3203	0.015	0.0413	7.23	0.1221
3	A3M5	179884	0.0015	1.3204	0.023	0.0415	6.75	0.1221
3	A3M6	179884	0.0025	1.3193	0.061	0.0502	12.2	0.1343
4	A4M1	109332	0.002	1.1786		0.6523		0.1373
4	A4M2	143852	0.002	1.1784	0.017	0.6479	0.68	0.1373
4	A4M3*	184652	0.002	1.1777	0.059	0.6448	0.48	0.1373
4	A4M4	233472	0.002	1.1769	0.068	0.6433	0.23	0.1373
4	A4M5	184652	0.0015	1.1773	0.034	0.6381	1.04	0.1424
4	A4M6	184652	0.0025	1.1777	0	0.6483	0.54	0.1465
5	A5M1	109332	0.002	1.1040		0.3070		0.1221
5	A5M2	143852	0.002	1.1020	0.181	0.2870	6.73	0.1221
5	A5M3*	186376	0.002	1.1008	0.109	0.2760	3.90	0.1221
5	A5M4	220856	0.002	1.1010	0.018	0.2796	1.30	0.1221
5	A5M5	186376	0.0015	1.1016	0.073	0.2782	0.79	0.1221
5	A5M6	186376	0.0025	1.1004	0.036	0.2757	0.11	0.1221

* The final case for analyses.

5 at $Re_D = 2 \times 10^5$. As seen from figure 2.6 the pressure drop (pressure difference between $\phi = 0$ and $\phi = 180$) over the cylinder changes as Reynolds number is increased from $Re_D = 1 \times 10^5$ to $Re_D = 2.6 \times 10^5$, while it is almost unchanged between $Re_D = 2.6 \times 10^5$ and $Re_D = 3.6 \times 10^6$. Schewe (2006) found the drag coefficient to be slightly reduced with the increase of Re_D , while Ong (2012) found the force to be close to constant as Reynolds number varied in the range of $1 \times 10^5 \leq Re_D \leq 4 \times 10^5$.

The present study show good agreement with the results found by Schewe (2006) and Ong (2012). The present results are also in good agreement with the remaining numerical and experimental results presented in figure 5.6.

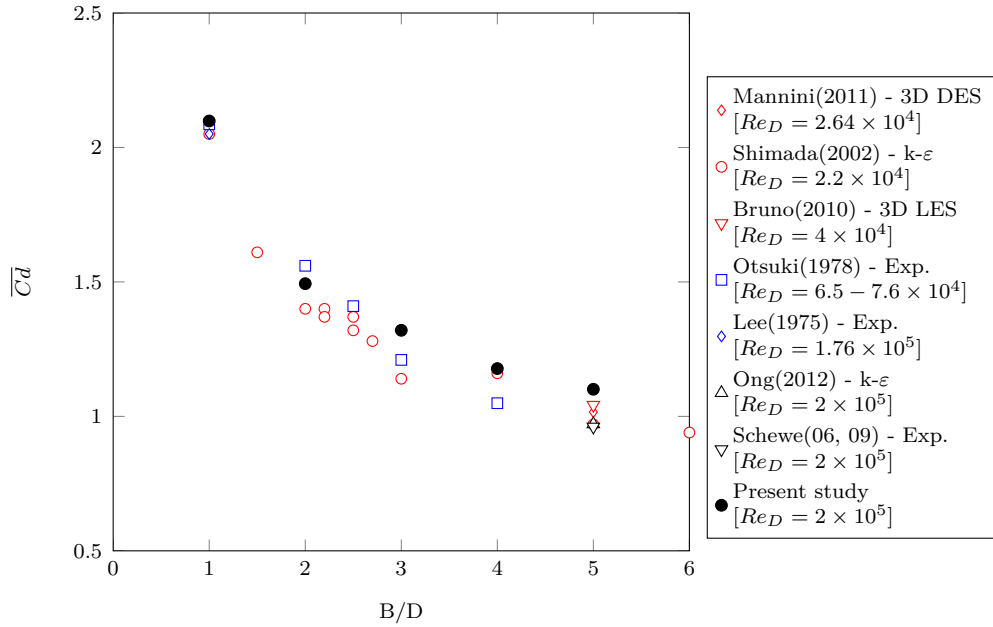


Figure 5.6: Variation of the mean drag coefficient according to aspect ratio

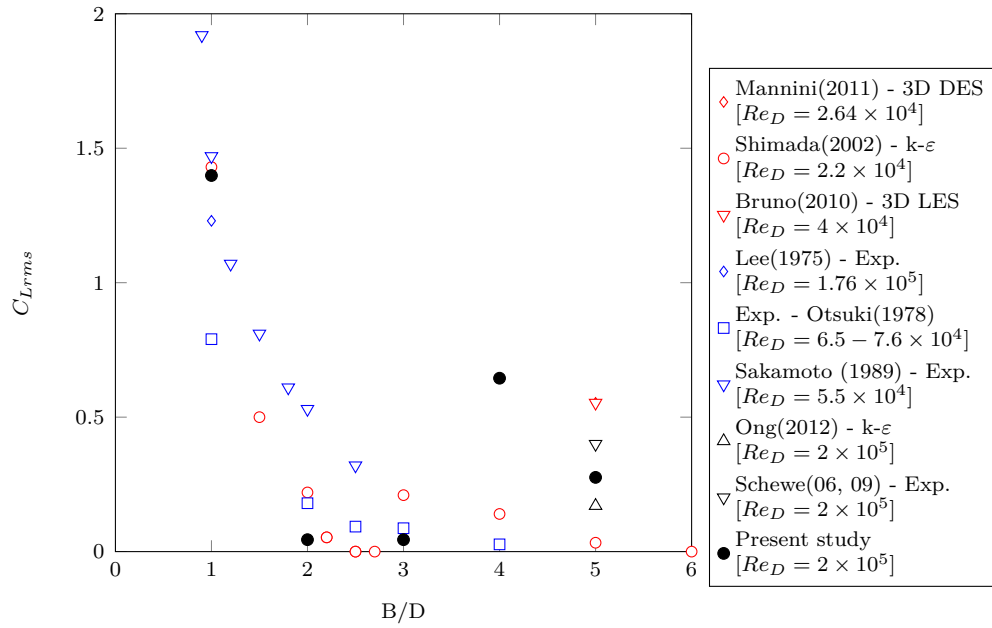


Figure 5.7: Variation of the RMS value of the lift coefficient according to aspect ratio

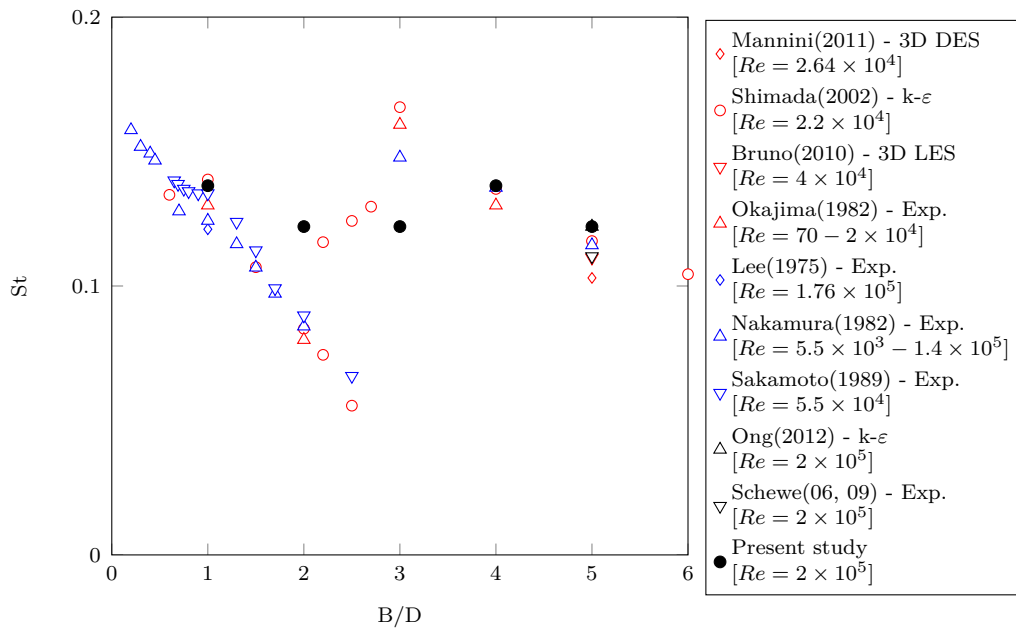


Figure 5.8: Variation of the Strouhal number according to aspect ratio

The RMS value of the lift coefficient

The present study shows strong aspect ratio dependence of the lift force. The largest RMS value of the lift coefficient is found for aspect ratio 1, while the smallest values are found for aspect ratio 2 and 3. As already mentioned the oscillations of the lift coefficient are very sensitive to the dynamics of the flow along the cylinder breadth. For this reason large disparities are found in the reference data.

A fluctuating behaviour of C_{Lrms} is present as the aspect ratio increases. Looking at the values of C_{Lrms} found by Otsuki et al. (1978) and Sakamoto et al. (1989) the coefficient decreases asymptotic with increasing aspect ratio. For the present study a stable reduction of the RMS value of the lift coefficient is present between aspect ratio 1, 4 and 5, but the values of C_{Lrms} for $B/D = 2$ and 3 deviate from this trend. A similar behaviour is found in the study of the aspect ratio dependency published by Shimada & Ishihara (2002).

Okajima (1983) (elaborated by Shimada & Ishihara (2002)) observed a double mode existing in the lift fluctuation for cross-sections with $2.0 < B/D < 2.8$ as a result of an unsteady reattachment of the separated shear layer. For $B/D = 2.8$ and 6.0 discontinuities in Strouhal number were apparent. This phenomenon challenged the development of numerical simulations for modelling flows around rectangular cross-sections. Shimada & Ishihara (2002) found the lift force to be zero for these aspect ratios. Double modes have not been seen in the present study.

Ong (2012) found that the C_{Lrms} is dependent of Reynolds number for $Re_D < 2 \times 10^5$. For $Re_D > 2 \times 10^5$ the variation of C_{Lrms} becomes small. A good agreement is found with results using the same Reynolds number.

The Strouhal number

The Strouhal number predicted from the present study alternates between the two values 0.1221 and 0.1373. This is caused by the reattachment of the separated shear layer, as elaborated later (see section 5.3.3). The realizations plotted in figure 5.8 show a decreasing Strouhal number as the aspect ratio increases in the separated-type cross-sections ($B/D < 2.8$). For the cross-sections in the range ($2.0 < B/D < 3.0$) a dispersion is present. As the aspect ratio is increased in the range $B/D \geq 3$, the Strouhal number decreases yet again.

It is seen that the Strouhal number is strongly dependent of the Reynolds number for the aspect ratios where reattachment is present. The breadth to depth ratios for which reattachment occurs are dependent on the Reynolds number. The

largest deviations compared to the reference values of lower Reynolds numbers are therefore found for aspect ratio 2 and 3.

The Strouhal number obtained in the present study fits well with published results of flow around the rectangular cylinder with aspect ratio 5 at Reynolds number $Re_D = 2 \times 10^5$.

5.3.2 Vorticity contours

Instantaneous vorticity contours of flow around the cylinders are shown in figure 5.9. All plots are of a fully developed flow. 40 contour levels from $\omega D/U_\infty = -50$ to $\omega D/U_\infty = 50$, where ω is the instantaneous vorticity, are plotted. All plots are from the time instant $tU_\infty/D = 300$. An identical color code is used for all plots. The red areas indicate the positive vorticity (counter-clockwise), while the blue indicate the negative vorticity (clockwise). The distance from the center of the cylinder to the end of the vortex street is $30D$ for all plots.

As seen from the figure, changing the aspect ratio will change the flow topology, the distance to where the first vortex is generated and the distance between the vortices. Also the length of the vortex street (i.e. the strength of the instantaneous vortices in the wake) differs.

The main parameter influencing the vortex heights is the depth of the cylinders. As long as the depths of the cylinders are unchanged, the heights of the vortices stay close to unchanged. The vortex centres are located close to the centreline of the cylinder due to symmetry.

For all aspect ratios the strongest vortices are found in the separated shear layer and along the cylinder sides. These vortices are generated by the no-slip condition of the cylinder surface. The separated shear layer rolls up and fades out in the wake. The longest vortex street is found for the square cylinder, for which the highest drag force is also found.

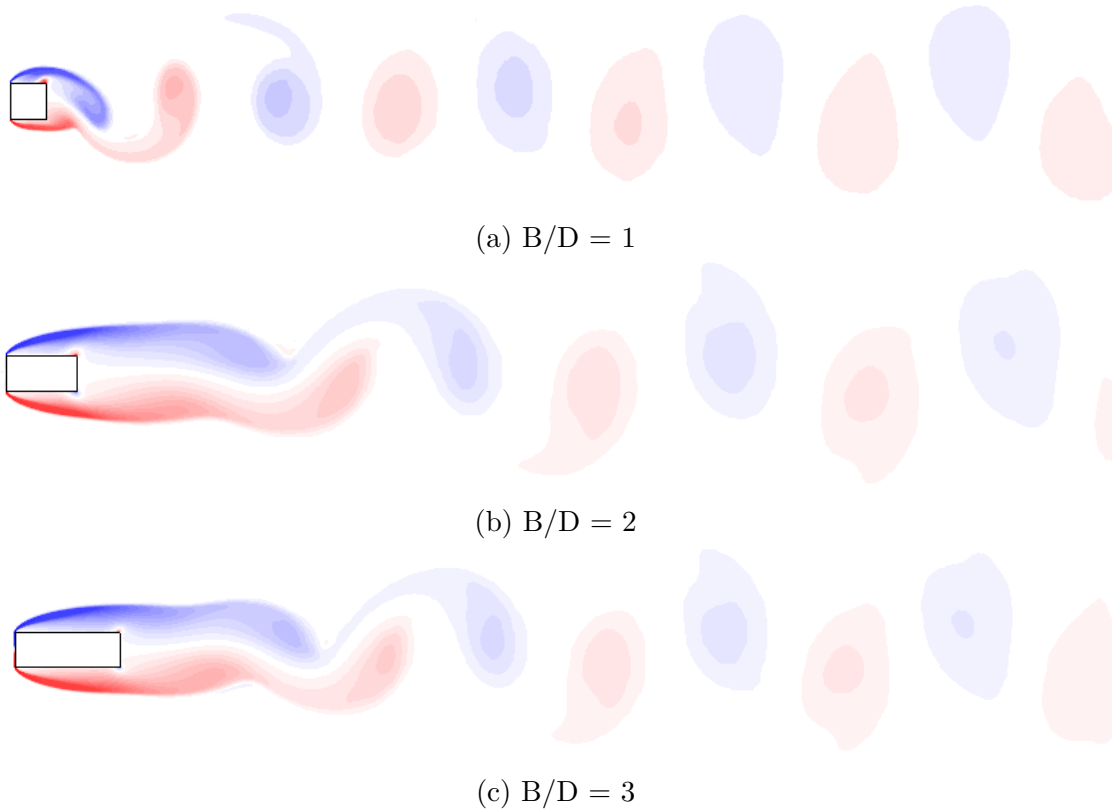
The vortex streets for the rectangular cylinders with aspect ratio 2 and 3 are close to identical. Both the length of the vortex street and the vortex shedding frequencies are close to equal. The location of the generation of the vortices is further downstream for the rectangular cylinder with $B/D = 2$.

The vortex street of the 4:1 rectangular cylinder is longer than vortex streets of its neighbouring aspect ratios. Similarities to the vortex streets of the square cylinder are seen. The shortest distance between the vortex centres and the high-

est vortex shedding frequencies appears for aspect ratios 1 and 4.

The shortest vortex street is found for $B/D = 5$, which also agrees with the drag coefficients found. It is seen from the figure that the distances between the vortices are highest for this aspect ratio.

The distance from the cylinder to the location of the generation of the vortices downstream of the cross-section decreases as the aspect ratio increases from $B/D = 2$ towards $B/D = 4$. For $B/D = 5$ the distance is increased, while the shortest distance to the cross-section is seen for the square cylinder. These locations are affected by the interaction between the separated shear layer and the rear corners. The vortices roll up as soon as the shear layer passes the rear side of the square cylinder. For the remaining rectangular cylinders the cylinder length and the presence of the rear corners keep the shear layers separated, forcing the vortex shedding process further downstream.



This figure continue on the next page

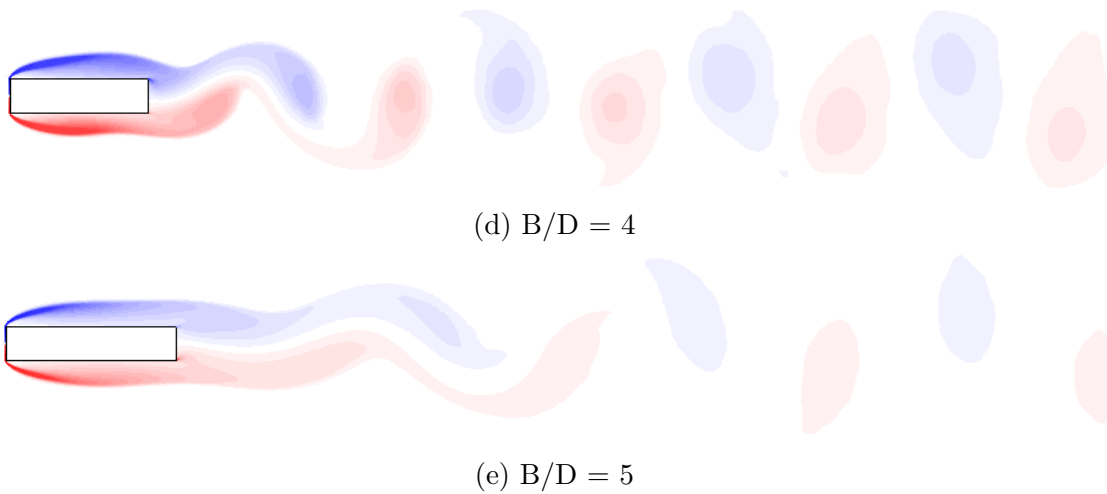


Figure 5.9: Instantaneous vorticity contours at $tU_\infty/D = 300$ for rectangular cylinders with aspect ratio 1, 2, 3, 4 and 5

5.3.3 Streamlines

Instantaneous streamlines over the 5:1 rectangular cylinder with a schematic overview of the mean flow structures are shown in figure 5.10. As the shear layer gets separated at the leading corner, the main vortex is formed along the cylinder side. Reattachment occurs at the end of the main vortex before the flow gets separated at the trailing corner. A reversed flow in the wake is generated.

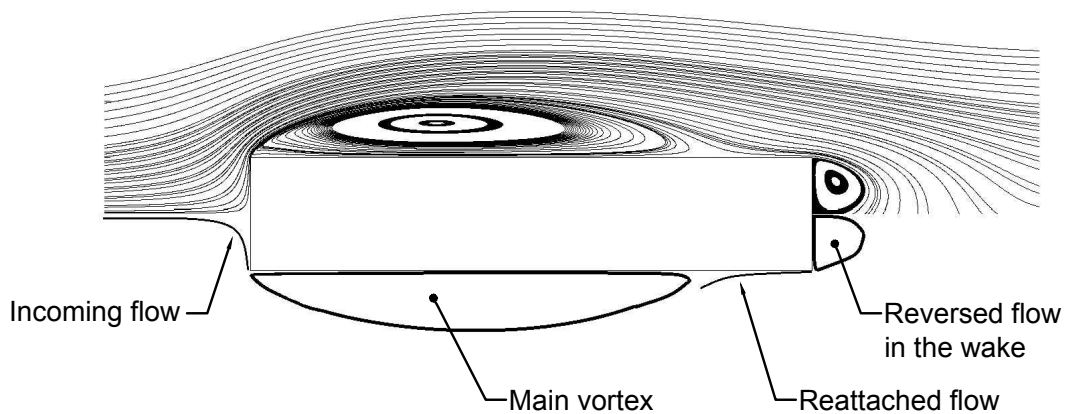


Figure 5.10: Schematic overview of mean flow structure

Instantaneous streamlines around the rectangular cylinders are shown in figure 5.13.

60 - 100 streamlines are plotted around each cylinder. The instantaneous streamlines from each cylinder are taken at the time instant $tU_\infty/D = 300$, as for the vorticity contours in figure 5.9. The distance from the center of the cylinder to the end of the figure is $15D$.

The main vortices acting on the square cylinder extend downstream of the cylinder sides. As a result, no reattachment is present. While an asymmetry of the vortices around the cylinder is present for the square cylinder, a symmetry is present for the main vortices acting on the $B/D = 2$ and 3 rectangular cylinders. These vortices are covering the whole length of the cylinder sides. The vortices are cut at the end of the cylinder, as illustrated by the red line in figure 5.11. As a result of the symmetry and main vortex length, the lift force acting on the cylinders is cancelled out.

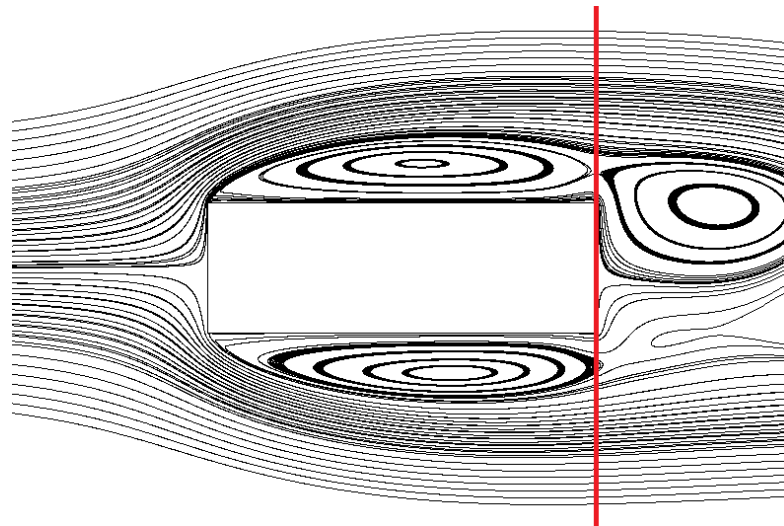


Figure 5.11: Symmetry in vortices around rectangular cylinder with aspect ratio 3

Reattachment is seen for the $B/D = 4$ and 5 rectangular cylinders. An imbalance in the main vortices is present. Figure 5.12 shows how the length of the main vortices around the cylinder changes length. These asymmetries are the main contribution for the lift force acting on the cylinders. The vortices in the reversed flow region fluctuate along the rear sides of the cylinders. This gives a frictional contribution to the lift force.

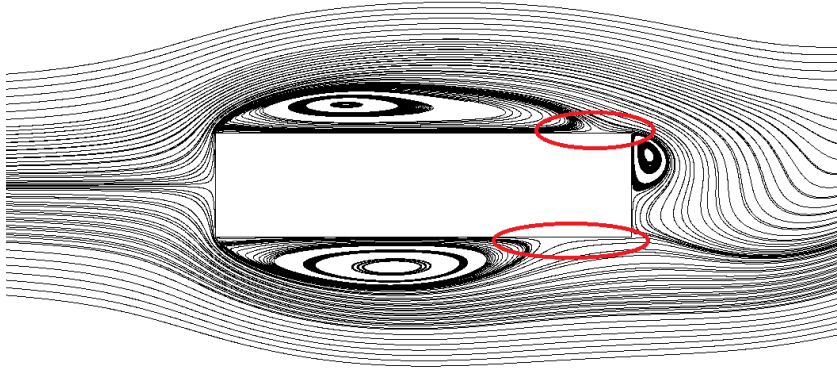


Figure 5.12: Asymmetry in vortices around rectangular cylinder with aspect ratio 4

The fluctuation of the vortex street is highest for the square cylinder. As the aspect ratio increases the vortex street gets flatter. This agrees with the length of the vortex street seen in figure 5.9.

As mentioned earlier, an alternating behaviour is seen for the Strouhal number. This is caused by the reattachment of the separated shear layer. The remaining length of the 4:1 rectangular cylinder downstream of the location of reattachment is close to equal the length of the square cylinder. For the 5:1 rectangular cylinder the remaining length downstream of the location of reattachment is close to equal the length of the 2:1 rectangular cylinder. For this reason the vortex shedding frequencies for rectangular cylinders with aspect ratio 1 and 4 are similar, and the vortex shedding frequencies for rectangular cylinders with aspect ratio 2, 3 and 5 are similar.

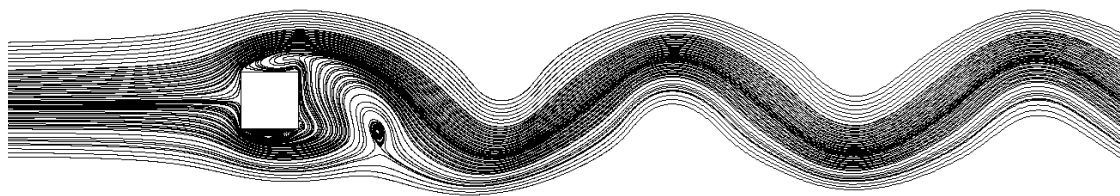
5.3.4 Pressure

Plots of the average pressure coefficient over the surfaces of the rectangular cylinders are shown in figure 5.15. The definition of S is seen in figure 1.2 on page 2. The coefficient is found using equation 5.1 on page 36. Some characteristics are seen for all plots:

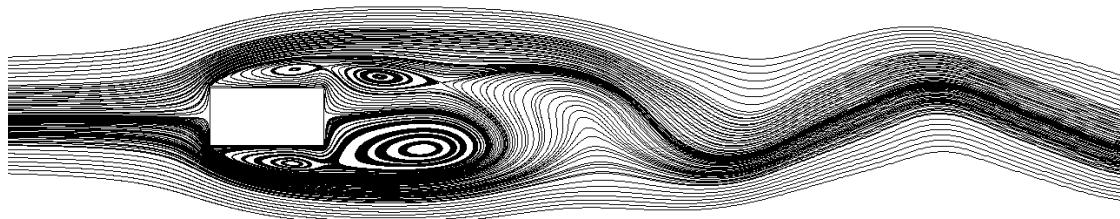
The mean pressure coefficient is 1 at the stagnation point ($S/D = 0$).

As the fluid flows from the stagnation point to the leading corner the velocity increases, and therefore the average pressure coefficient decreases.

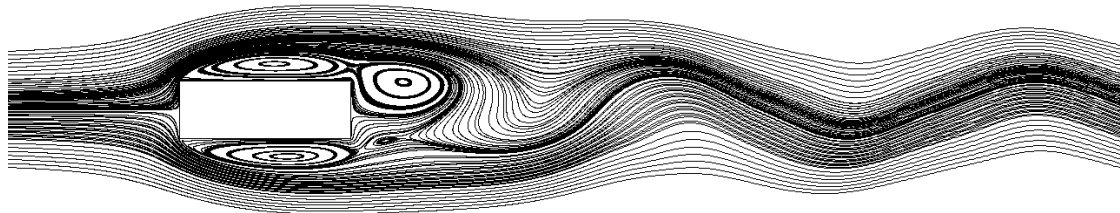
At the leading corner a negative $\overline{C_P}$ is seen.



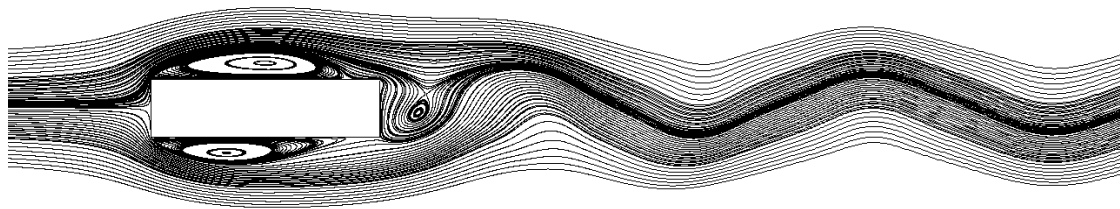
(a) $B/D = 1$



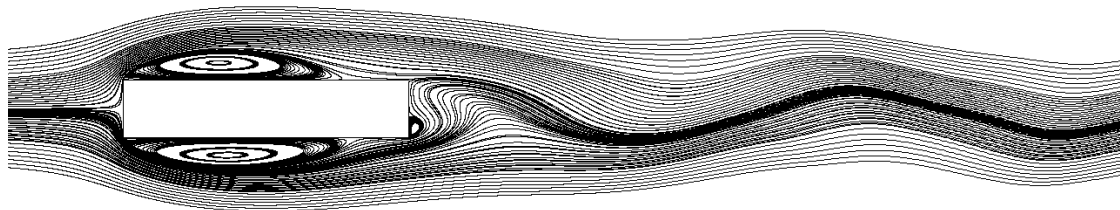
(b) $B/D = 2$



(c) $B/D = 3$



(d) $B/D = 4$



(e) $B/D = 5$

Figure 5.13: Instantaneous streamlines at $tU_\infty/D = 300$ for rectangular cylinders with aspect ratio 1, 2, 3, 4 and 5

From the leading to the trailing corner the velocity is slowed down, resulting in a increase of average pressure coefficient.

A change in the pressure is present around the trailing corner. This is a result of a change of the velocity around the trailing corner.

The largest pressure difference between the mean pressure coefficient at the stagnation point and the leading corner is found for the square cylinder. The average pressure distributions of the $B/D = 2$ and 3 rectangular cylinders are showing a correlation. The mean pressure coefficient stays close to constant from the leading to the trailing corner. Around the trailing corner the mean pressure coefficient increases. For the rectangular cylinders with aspect ratio 4 and 5, $\overline{C_P}$ increases as the fluid particles flows from the leading corner to the trailing corner and decreases around the trailing corner.

The mean base pressure coefficients against aspect ratio are plotted in figure 5.14. As seen from the plot the coefficient increases with increasing aspect ratio.

Instantaneous and averaged pressure contours from the present simulations are shown in appendix B.

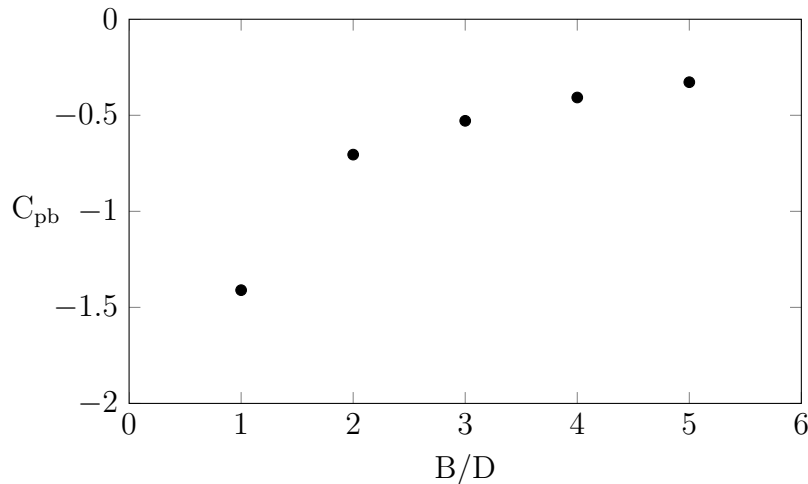


Figure 5.14: Variation of mean base pressure coefficients according to aspect ratio

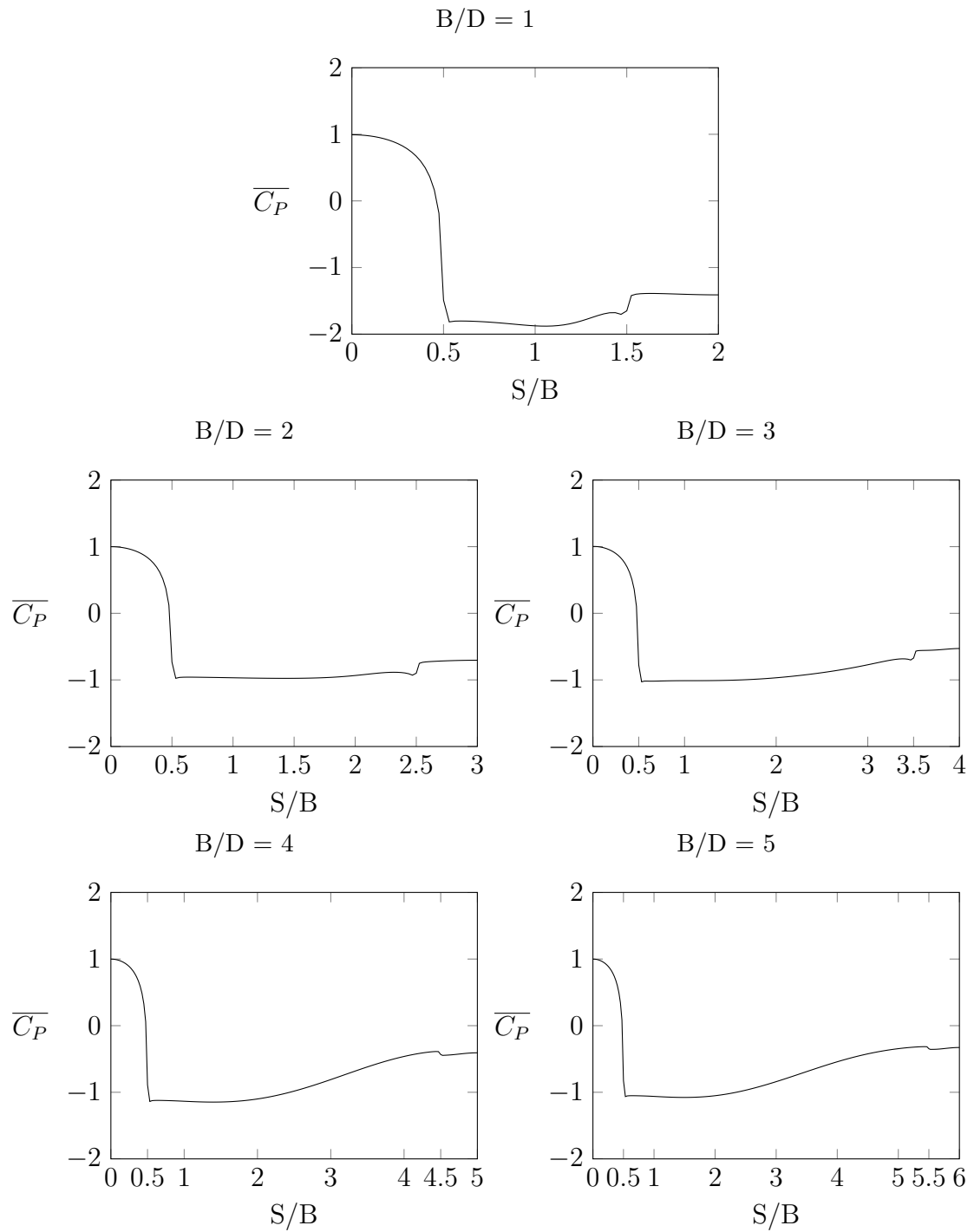


Figure 5.15: Time-averaged pressure distributions on the surfaces of rectangular cylinders with aspect ratio 1, 2, 3, 4 and 5

5.3.5 Velocity distribution

The mean streamwise velocity distributions along the centrelines of the rectangular cylinders are shown in figure 5.17. The velocity distributions upstream of the cylinder are close to identical for all aspect ratios in the present study. As the fluid flow approaches the cylinder the velocity declines toward the stagnation point. The length of the rectangular cylinder does not influence the velocity field upstream of the cylinder.

Downstream of the cylinders disparities in the mean streamwise velocity distributions are present. The length of the cylinder clearly influences the velocity distributions. For aspect ratio 1 the \overline{U}_1 is quickly recovered towards the inlet velocity. For the remaining aspect ratios a slower recovery is present.

The lengths of the mean recirculation regions against aspect ratio are plotted in figure 5.16. As seen from the plot the length of the recirculation region is corresponding to the distance from the cylinder to the location of generation of the vortices.

Instantaneous and mean contours of the streamwise velocity component from the present simulations are shown in appendix C.

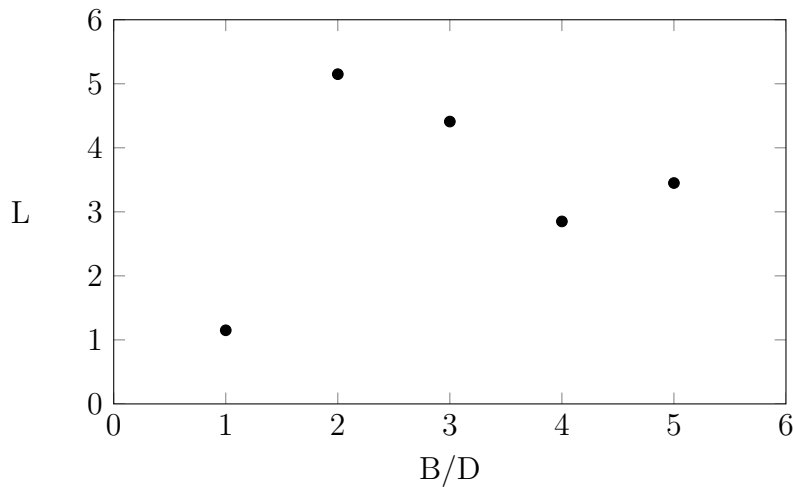


Figure 5.16: Variation of length of the mean recirculation region according to aspect ratio

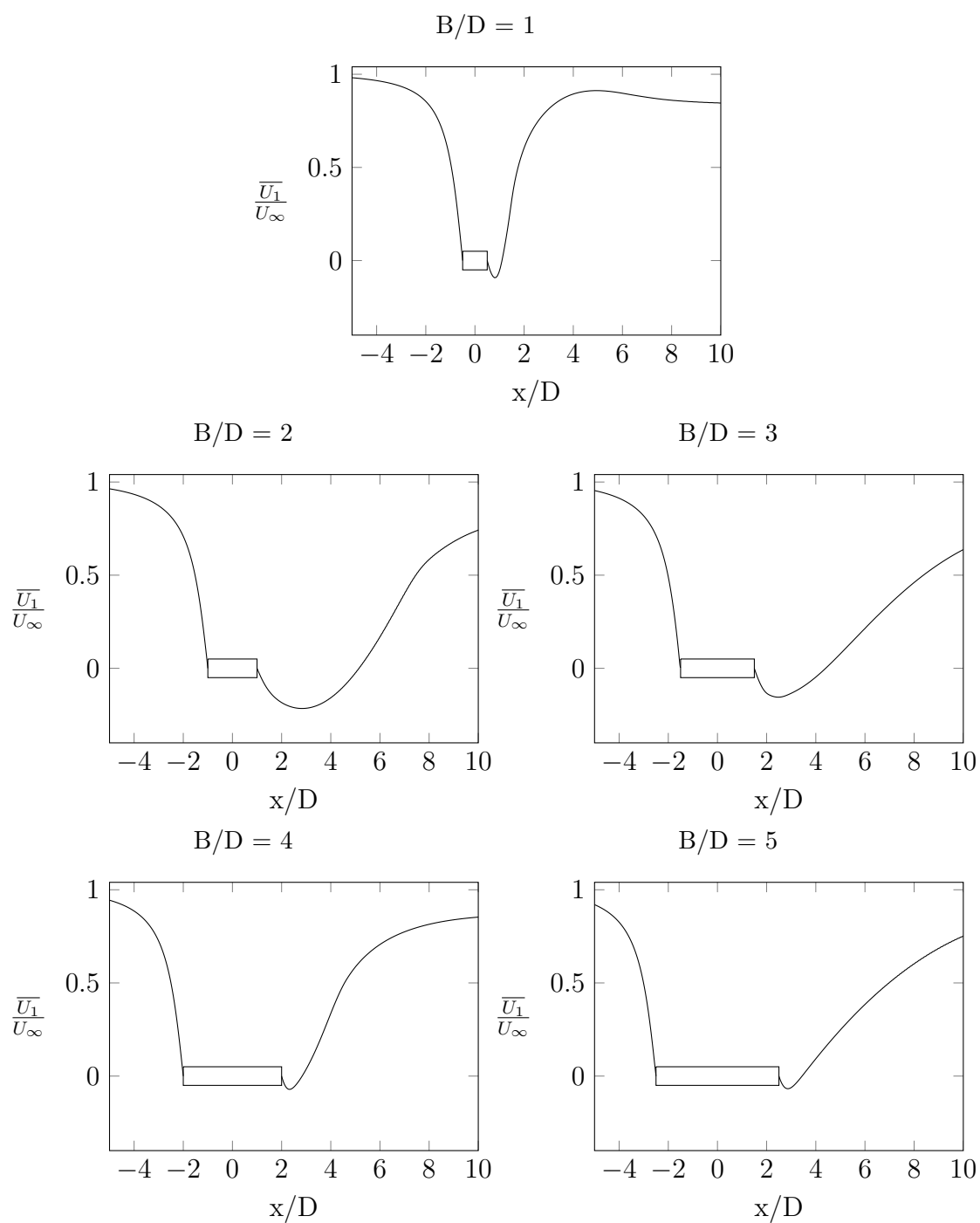


Figure 5.17: Mean streamwise velocity distribution along the centreline of rectangular cylinders with aspect ratio 1, 2, 3, 4 and 5

6 Conclusion

Computations of flows at high Reynolds number around rectangular cylinders with different aspect ratios have been performed by the use of the 2D URANS method with a standard high Reynolds number $k-\varepsilon$ turbulence model. The aspect ratios investigated were $B/D = 1, 2, 3, 4, 5$. The Reynolds number based on the cylinder height was set to $Re_D = 2 \times 10^5$ for all aspect ratios.

The rectangular cylinder of aspect ratio 5 has been used for the purpose of validating the applicability of the 2D URANS method with the standard high Reynolds number $k-\varepsilon$ turbulence model. The model showed a good agreement for $\overline{C_D}$, C_{Lrms} and St with published numerical and experimental data at the same Reynolds number. The mean pressure distribution around the cylinder was in relatively good agreement with numerical and experimental data. It was concluded that the model is reliable for calculating the flow at a high Reynolds number around the 5:1 rectangular cylinders.

Parameter studies were performed for the grid and the time step for all aspect ratios studied in the thesis. The hydrodynamic quantities showed a strong dependency of both the grid and time step. Configurations giving sufficient numerical accuracy were found for all aspect ratios.

For the rectangular cylinder with aspect ratio 5, the presently predicted $\overline{C_D}$, C_{Lrms} and St are in good agreement with published experimental and numerical data at the same Reynolds number. For the rectangular cylinders with aspect ratio 1, 2, 3 and 4, a higher number of realizations at $Re_D = 2 \times 10^5$ are needed for a thoroughly validation of the model.

The results calculated in the present study have reproduced the physics in a reasonable manner. The mean drag coefficients were found to be in a good agreement with both 2D and 3D numerical simulations, and experiments found at lower Reynolds numbers, while disparities were present for C_{Lrms} and St . A symmetry was found in the vortices around the rectangular cylinders with aspect ratio 2 and

3. As a result the C_{Lrms} were found to be close to zero. The predicted Strouhal numbers were found to be $St = 0.1373$ for $B/D = 1$ and 4, and $St = 0.1221$ for $B/D = 2, 3$ and 5. It was concluded that this alternating behaviour is a result of the reattachment of the flow.

The 3D effects from turbulence seem to have an insignificant influence in the studied problem for the numerical models currently available. The simplifications the turbulence model introduces seem to give the same order of error as uncertainties in experimental set-up and the numerical LES and DES simulations.

The reattachment of the separated shear layer is in the present study found to be in the range $3 < B/D < 4$ for $Re_D = 2 \times 10^5$. A bimodal vortex shedding was not found to exist in the present configurations.

From the data, it may be concluded that the results from the present study can be useful for engineering design purposes.

7 Recommendations for Further Work

Even though flow around cylindrical structures has been a classical subject in hydrodynamics, it is still an interesting field to investigate and study.

The lack of published data for flows around rectangular cylinders with Reynolds number $Re_D = 2 \times 10^5$ have made it difficult to perform a detailed validation of the model. The author would like to see results from laboratory tests for the present studied configurations. It would be interesting to compare the results obtained with another numerical method or another turbulence model using the same configurations, e.g. LES, DES, $k-\omega$ URANS. It would also be interesting to investigate the influence of 3D effects by performing the analysis of the same configurations in a three dimensional domain.

In the present study the values for the aspect ratios where unsteady reattachment of the separated shear layer occurs were not found. A study of aspect ratios in the range of $3 < B/D < 4$ to investigate the reattachment of the separated shear layer would be of interest. As mentioned the unsteady reattachment of the separated shear layer is found to occur for aspect ratios in the range of $2 < B/D < 3$ for flows with Reynolds number $Re_D = 2.2 \times 10^4$ (Shimada & Ishihara 2002). It would be interesting to study this phenomenon in a range of high Reynolds numbers.

The present study can be used as a preliminary study for investigation of flow around rectangular cylinders of various aspect ratio near to a wall. This would be an interesting topic of investigation.

Bibliography

- Bakker, A. (2006), *Lecture 7 - Meshing*, lecture notes distributed in Computational Fluid Dynamics (ENGS 150) at Dartmouth College, accessed 10 June 2014, <http://www.bakker.org/dartmouth06/engs150/07-mesh.pdf>.
- Bartoli, G., Borsani, A., Mannini, C., Marra, A., Procino, L. & Ricciardelli, F. (2011), Wind tunnel study on the aerodynamics of a 5:1 rectangular cylinder in smooth flow, *in* 'Proceedings of the Thirteenth International Conference on Wind Engineering, Amsterdam, The Netherlands'.
- Bartoli, G., Bruno, L., Buresti, G., Ricciardelli, F., Salvetti, M. & Zasso, A. (2008), 'Barc overview document'. (Accessed 1 February 2014).
URL: <http://www.aniv-iawe.org/barc>
- Bruno, L., Fransos, D., Coste, N. & Bosco, A. (2010), '3D flow around a rectangular cylinder: A computational study', *Journal of Wind Engineering and Industrial Aerodynamics* **98**(6), 263–276.
- Bruno, L., Salvetti, M. V. & Ricciardelli, F. (2014), 'Benchmark on the Aerodynamics of a Rectangular 5:1 Cylinder: An overview after the first four years of activity', *Journal of Wind Engineering and Industrial Aerodynamics* **126**, 87–106.
- Ferziger, J. & Perić, M. (2002), *Computational Methods for Fluid Dynamics*, 3th edition edn, Springer Berlin.
- Galli, F. (2005), 'Comportamento aerodinamico di strutture snelle non profilate: approccio sperimentale e computazionale', *Master's Thesis, Politecnico di Torino, Turin, Italy (in Italian)* .
- HighComp (2014), 'Offshore/Subsea'. (Accessed 10 June 2014).
URL: http://highcomp.no/wp-content/uploads/2013/03/CAD_field-1024x568.jpg

-
- Homem-Christo, G. H., Bangalter, T. & Bridges, J. (2010), *The Grid*, Walt Disney Records.
- Launder, B. & Sharma, B. (1974), ‘Application of the energy-dissipation model of turbulence to the calculation of flow near a spinning disc’, *Letters in Heat and Mass Transfer* **1**(2), 131–137.
- Lee, B. E. (1974), ‘The effect of turbulence on the surface pressure field of a square prism’, *Journal of Fluid Mechanics* **69**(02), 263.
- Mannini, C., Šoda, A. & Schewe, G. (2010), ‘Unsteady RANS modelling of flow past a rectangular cylinder: Investigation of Reynolds number effects’, *Computers & Fluids* **39**(9), 1609–1624.
- Mannini, C., Šoda, A. & Schewe, G. (2011), ‘Numerical investigation on the three-dimensional unsteady flow past a 5:1 rectangular cylinder’, *Journal of Wind Engineering and Industrial Aerodynamics* **99**(4), 469–482.
- Matsumoto, M. (2005), via Mannini et al. (2010) through their personal communication.
- Nakamura, Y. & Yoshimura, T. (1982), ‘Flutter and vortex excitation of rectangular prisms in pure torsion in smooth and turbulent flows’, *Journal of Sound and Vibration* **84**(3), 305–317.
- Norwegian Public Roads Administration (2012), ‘Project overview - costal highway route e39’. (Accessed 10 June 2014).
URL: http://www.vegvesen.no/_attachment/300340/binary/527486?fast_title=Ferjefri+E39+summary+January+2012+%28English%29.pdf
- Okajima, A. (1982), ‘Strouhal numbers of rectangular cylinders’, *Journal of Fluid Mechanics* **123**(-1), 379.
- Okajima, A. (1983), ‘Flow around a rectangular cylinder with a section of various width/height ratios’, *Journal of Wind Engineering* **17**, 1–19 (in Japanese).
- Ong, M. C. (2012), Unsteady RANS Simulation of Flow Around a 5:1 Rectangular Cylinder at High Reynolds Numbers, in ‘Volume 5: Ocean Engineering; CFD and VIV’, ASME, pp. 841–846.
- OpenFOAM Ltd. (2014), ‘OpenFOAM User Guide’. (Accessed 10 June 2014).
URL: <http://www.openfoam.org/docs/user/>

- Otsuki, Y., Washizu, K. & Ohya, A. (1978), Wind tunnel experiments on aerodynamic forces and pressure distributions of rectangular cylinders in a uniform flow, *in* ‘Proceedings of the Fifth Symposium on Wind Effects on Structures’, pp. 169–176.
- Pope, S. (2000), *Turbulent Flows*, Cambridge University Press.
- Sakamoto, H., Haniu, H. & Kobayashi, Y. (1989), ‘Fluctuating force action on rectangular cylinders in uniform flow (on rectangular cylinders with fully separated flow)’, *Transactions of the Japan Society of Mechanical Engineers, Series B* **55**(516), 2310–2317.
- Schewe, G. (2006), Influence of the Reynolds-number on flow-induced vibrations of generic bridge sections, *in* ‘Proceedings of the International Conference on Bridges’, Dubrovnik, Croatia, pp. 351–358.
- Schewe, G. (2009), Reynolds-number-effects in flow around a rectangular cylinder with aspect ratio 1:5, *in* ‘Proceedings of the 5th European and African Conference on Wind Engineering’, Firenze University Press, Florence, Italy.
- Schlichting, H. & Gersten, K. (2000), *Boundary Layer Theory*, 8th edition edn, Springer Berlin Heidelberg.
- Shimada, K. & Ishihara, T. (2002), ‘Application Of A Modified $k-\epsilon$ Model To The Prediction Of Aerodynamic Characteristics Of Rectangular Cross-Section Cylinders’, *Journal of Fluids and Structures* **16**(4), 465–485.
- Spalart, P., Jou, W.-H., Strelets, M. & Allmaras, S. (1997), Comments on the Feasibility of LES for Wings, and on a Hybrid RANS/LES Approach, *in* ‘Proceedings of the First AFOSR International Conference on DNS/LES’.
- Sumer, B. M. & Fredsoe, J. (2006), *Hydrodynamics Around Cylindrical Structures (Advanced Series on Ocean Engineering)*, World Scientific Pub Co Inc.
- Teknisk Ukeblad (2012), ‘Disse gigantbruene skal gjøre fjordene fergefrie’. (Accessed 10 June 2014).
URL: <http://www.tu.no/incoming/2012/11/22/1200011501.jpg/alternates/w1366f/1200011501.jpg>
- Versteeg, H. & Malalasekera, W. (2007), *An Introduction to Computational Fluid Dynamics: The Finite Volume Method (2nd Edition)*, Prentice Hall.
- Yu, D. & Kareem, A. (1998), ‘Parametric study of flow around rectangular prisms using LES’, *Journal of Wind Engineering and Industrial Aerodynamics* **77** & **78**, 653–662.

Appendices

A Simulation Control Files

A.1 controlDict

```
1  /*----- C++ -----*/
2  |-----|
3  | \ \ \ \ \ | F i e l d | | OpenFOAM: The Open Source CFD Toolbox |
4  | \ \ \ \ \ | O p e r a t i o n | | Version: 1.6 |
5  | \ \ \ \ \ | A n d | | Web: www.OpenFOAM.org |
6  | \ \ \ \ \ | M a n i p u l a t i o n | |-----|
7  /*-----*/
8  FoamFile
9  {
10     version      2.0;
11     format        ascii;
12     class         dictionary;
13     location      "system";
14     object        controlDict;
15 }
16 // *****
17
18 application      pisoFoam;
19
20 startFrom        latestTime;
21
22 startTime        0;
23
24 stopAt           endTime;
25
26 endTime          300;
27
28 deltaT           0.002;
29
30 writeControl     runtime;
31
32 writeInterval    1;
33
34 purgeWrite       0;
35
36 writeFormat      ascii;
37
38 writePrecision   6;
39
40 writeCompression compressed;
41
42 timeFormat       general;
```

```

43 |
44 | timePrecision 6;
45 |
46 | runTimeModifiable no;
47 |
48 | functions
49 | (
50 |     forces
51 |     {
52 |     type forces;
53 |     functionObjectLibs ("libforces.so");
54 |     patches (CYLINDER);
55 |     pName p;
56 |     UName U;
57 |     log false;
58 |     rhoName rhoInf;
59 |     rhoInf 1000;
60 |     CofR (0 0 0);
61 |     outputControl timeStep;
62 |     outputInterval 1;
63 |     }
64 |
65 |     forceCoeffs
66 |     {
67 |     type forceCoeffs;
68 |     functionObjectLibs ("libforces.so");
69 |     outputControl timeStep;
70 |     outputInterval 1;
71 |     patches (CYLINDER);
72 |     pName p;
73 |     UName U;
74 |     log false;
75 |     rhoName rhoInf;
76 |     rhoInf 1000;
77 |     CofR (0 0 0);
78 |     liftDir (0 1 0);
79 |     dragDir (1 0 0);
80 |     pitchAxis (0 0 1);
81 |     magUInf 1;
82 |     lRef 1;
83 |     Aref 0.894427;
84 |     }
85 |
86 |     fieldAverage1
87 |     {
88 |     type fieldAverage;
89 |     functionObjectLibs ( "libfieldFunctionObjects.so" );
90 |     enabled true;
91 |     outputControl outputTime;
92 |     fields
93 |     (
94 |         U
95 |         {
96 |             mean on;
97 |             prime2Mean on;
98 |             base time;
99 |         }
100 |
101 |         p
102 |         {
103 |             mean on;
104 |             prime2Mean on;

```

```

105         base      time;
106     };
107 };
108 }
109
110 );
111
112 // *****

```

A.2 fvSchemes

```

1  /*----- C++ -----*/
2  |-----|
3  | \ \ \ \ | F i e l d | OpenFOAM: The Open Source CFD Toolbox
4  | \ \ \ \ | O p e r a t i o n | Version: 1.6
5  | \ \ \ \ | A n d | Web: http://www.OpenFOAM.org
6  | \ \ \ \ | M a n i p u l a t i o n |
7  |-----|
8  FoamFile
9  {
10     version      2.0;
11     format        ascii;
12     class         dictionary;
13     object        fvSchemes;
14 }
15 // *****
16
17 ddtSchemes
18 {
19     default       CrankNicolson 0.5;
20 }
21
22 gradSchemes
23 {
24     default       Gauss linear;
25     grad(p)       Gauss linear;
26     grad(U)       Gauss linear;
27 }
28
29 divSchemes
30 {
31     default       none;
32     div(phi,U)    Gauss limitedLinearV 1;
33     div(phi,k)    Gauss limitedLinear 1;
34     div(phi,epsilon) Gauss limitedLinear 1;
35     div(phi,R)    Gauss limitedLinear 1;
36     div(R)        Gauss linear;
37     div(phi,nuTilda) Gauss limitedLinear 1;
38     div((nuEff*dev(T(grad(U)))) Gauss linear;
39 }
40
41 laplacianSchemes
42 {
43     default       none;
44     laplacian(nuEff,U) Gauss linear corrected;
45     laplacian((1|A(U)),p) Gauss linear corrected;

```

```

46     laplacian(DkEff,k) Gauss linear corrected;
47     laplacian(DepsilonEff,epsilon) Gauss linear corrected;
48     laplacian(DREff,R) Gauss linear corrected;
49     laplacian(DnuTildaEff,nuTilda) Gauss linear corrected;
50 }
51
52 interpolationSchemes
53 {
54     default          linear;
55     interpolate(U)   linear;
56 }
57
58 snGradSchemes
59 {
60     default          corrected;
61 }
62
63 fluxRequired
64 {
65     default          no;
66     p                ;
67 }
68
69 // ***** //

```

A.3 fvSolution

```

1  /*-----* C++ *-----*/
2  |-----|
3  | \ \ \ \ | F i e l d | OpenFOAM: The Open Source CFD Toolbox |
4  | \ \ \ \ | O p e r a t i o n | Version: 1.6 |
5  | \ \ \ \ | A n d | Web: www.OpenFOAM.org |
6  | \ \ \ \ | M a n i p u l a t i o n |-----|
7  /*-----*/
8  FoamFile
9  {
10     version      2.0;
11     format       ascii;
12     class        dictionary;
13     location     "system";
14     object       fvSolution;
15 }
16 // ***** //
17
18 solvers
19 {
20     p
21     {
22         solver      PCG;
23         preconditioner DIC;
24         tolerance   1e-06;
25         relTol      0;
26     }
27
28     pFinal
29     {

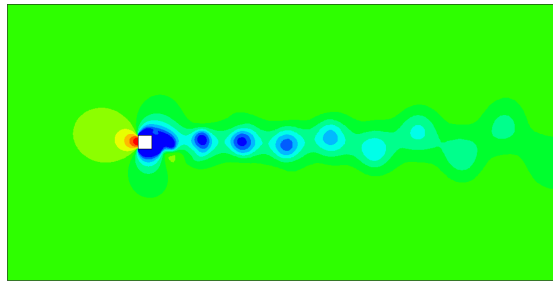
```

```

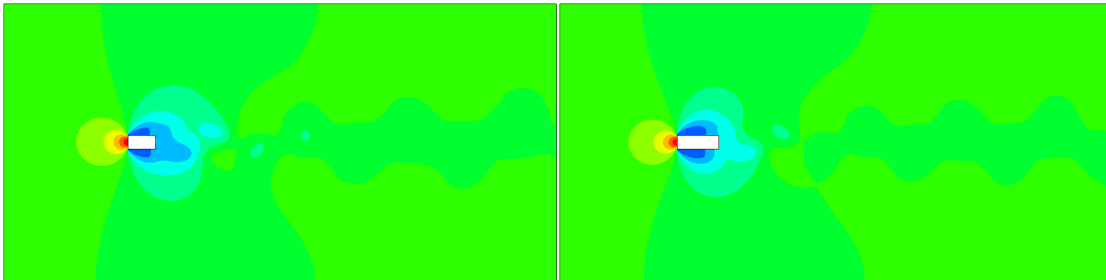
30     solver          PCG;
31     preconditioner  DIC;
32     tolerance       1e-06;
33     relTol          0;
34 }
35
36 U
37 {
38     solver          PBiCG;
39     preconditioner  DILU;
40     tolerance       1e-05;
41     relTol          0;
42 }
43
44 k
45 {
46     solver          PBiCG;
47     preconditioner  DILU;
48     tolerance       1e-05;
49     relTol          0;
50 }
51
52 epsilon
53 {
54     solver          PBiCG;
55     preconditioner  DILU;
56     tolerance       1e-05;
57     relTol          0;
58 }
59
60 R
61 {
62     solver          PBiCG;
63     preconditioner  DILU;
64     tolerance       1e-05;
65     relTol          0;
66 }
67
68 nuTilda
69 {
70     solver          PBiCG;
71     preconditioner  DILU;
72     tolerance       1e-05;
73     relTol          0;
74 }
75 }
76
77 PISO
78 {
79     nCorrectors      2;
80     nNonOrthogonalCorrectors 3;
81 }
82
83 // ***** //

```


B Pressure distribution

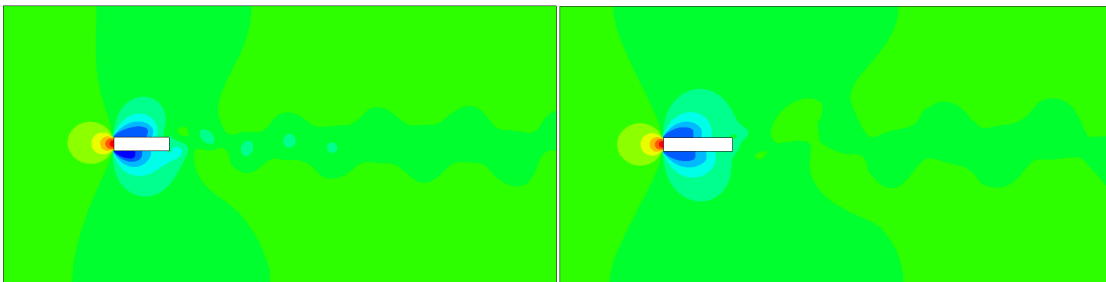


(a) $B/D = 1$



(b) $B/D = 2$

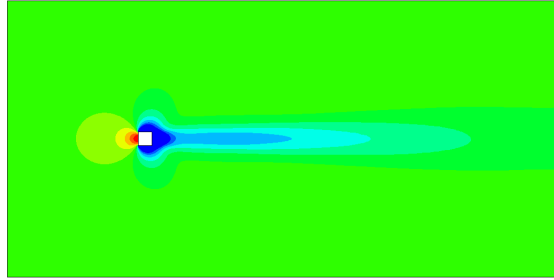
(c) $B/D = 3$



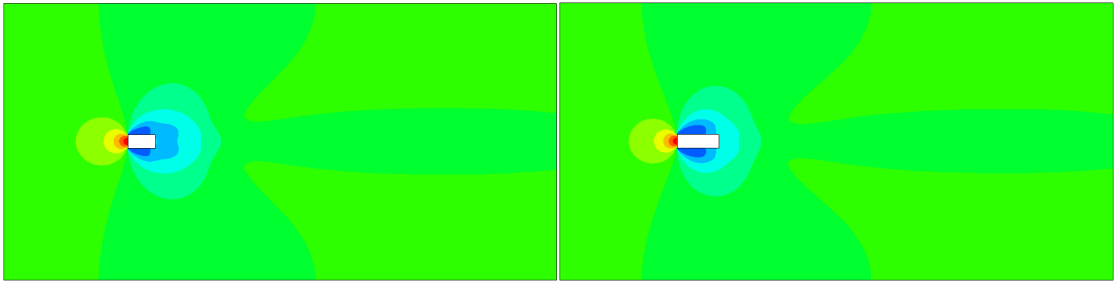
(d) $B/D = 4$

(e) $B/D = 5$

Figure B.1: Instantaneous pressure contours at $tU_\infty/D = 300$ for the rectangular cylinders with aspect ratio 1, 2, 3, 4 and 5. Red colors indicate positive pressure, while blue indicate negative pressure.

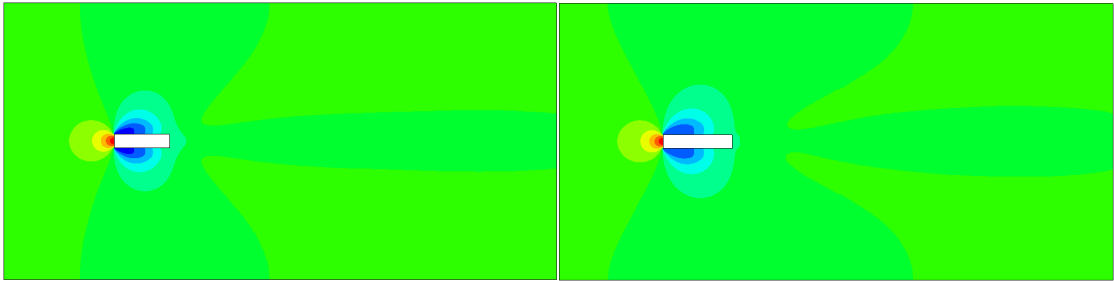


(a) $B/D = 1$



(b) $B/D = 2$

(c) $B/D = 3$

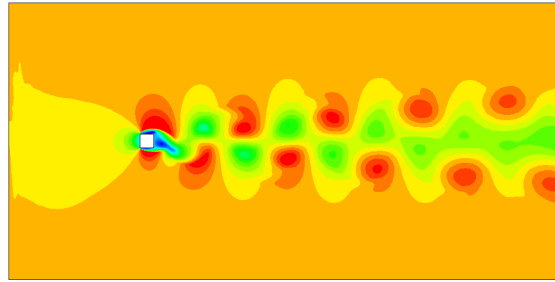


(d) $B/D = 4$

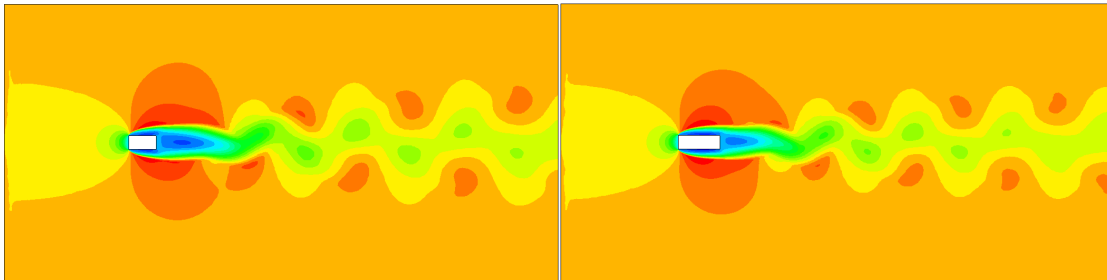
(e) $B/D = 5$

Figure B.2: Averaged pressure contours for the rectangular cylinders with aspect ratio 1, 2, 3, 4 and 5. Red colors indicate positive pressure, while blue indicate negative pressure.

C Velocity contours

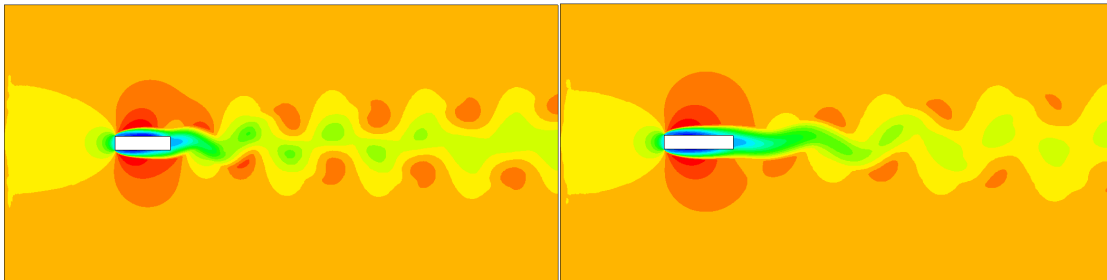


(a) $B/D = 1$



(b) $B/D = 2$

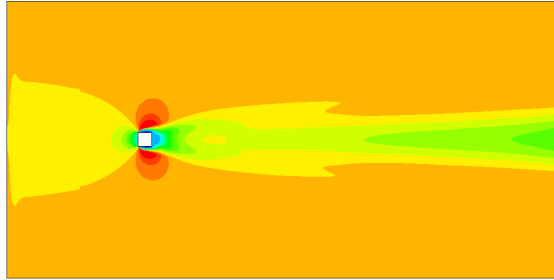
(c) $B/D = 3$



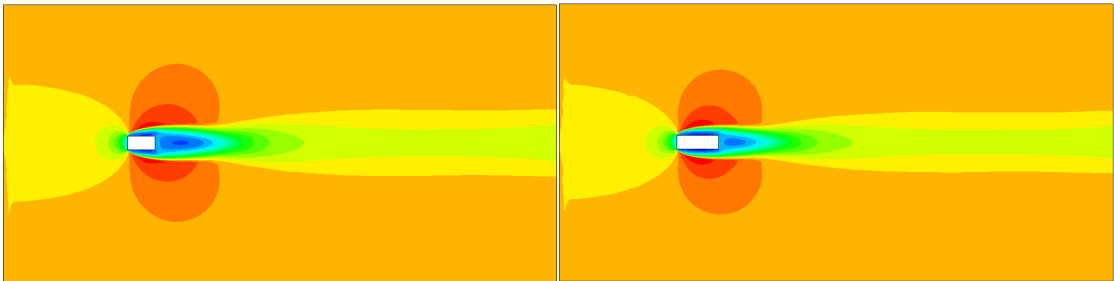
(d) $B/D = 4$

(e) $B/D = 5$

Figure C.1: Instantaneous velocity contours at $tU_\infty/D = 300$ for rectangular cylinders with aspect ratio 1, 2, 3, 4 and 5. Red colors indicate positive velocity, while blue indicate negative velocity.

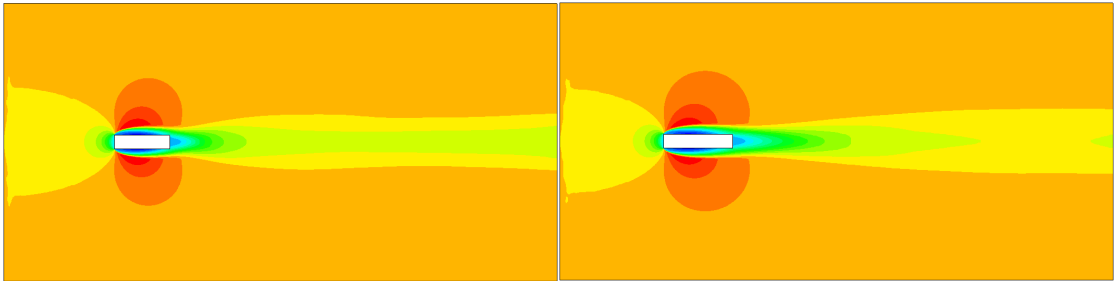


(a) $B/D = 1$



(b) $B/D = 2$

(c) $B/D = 3$



(d) $B/D = 4$

(e) $B/D = 5$

Figure C.2: Mean velocity contours for rectangular cylinders with aspect ratio 1, 2, 3, 4 and 5. Red colors indicate positive velocity, while blue indicate negative velocity.